

Role of defects in the thermodynamic stability of grain boundary phases at asymmetric tilt boundaries in copper

Swetha Pemma^{a,1}, Lena Langenohl^a, Saba Saood^a, Yoonji Choi^a, Rebecca Janisch^b, Christian H. Liebscher^{a,c,d}, Gerhard Dehm^{a,*}, Tobias Brink^{a,*}

^aMax Planck Institute for Sustainable Materials, Max-Planck-Straße 1, 40237 Düsseldorf, Germany

^bInterdisciplinary Centre for Advanced Materials Simulation (ICAMS), Ruhr-Universität Bochum, 44780 Bochum, Germany

^cResearch Center Future Energy Materials and Systems, Ruhr-Universität Bochum, 44801 Bochum, Germany

^dFaculty of Physics and Astronomy, Ruhr-Universität Bochum, 44801 Bochum, Germany

Abstract

Grain boundaries can exist as different grain boundary phases (also called complexions) with individual atomic structures. The thermodynamics of these defect phases in high-angle grain boundaries were studied mostly with atomistic and phase field computer simulations, but almost exclusively for special, symmetric boundaries. Here, we use molecular dynamics simulations combined with structure search methods, as well as scanning transmission electron microscopy experiments to take a step towards understanding more general grain boundaries. Using the example of $\Sigma 37c$ [11\bar{1}] tilt boundaries in Cu, we show how the grain boundary phase transition on a symmetric boundary plane is changed by the geometrically necessary defects introduced in inclined, asymmetric boundaries. We analyze the disconnections—which are dislocation-like line defects of grain boundaries—both in the simulations, as well as in experimental Cu and Al samples. A main finding is that defect energies can have a major influence on the stability of grain boundary phases, even at small inclinations. Furthermore, some defects are not able to effect large inclinations. At that point, defective asymmetric GB phases compete with grain boundaries faceting into the adjacent symmetric GB phases.

Keywords: Grain boundary phases, Molecular dynamics, Scanning transmission electron microscopy

1. Introduction

Grain boundaries (GBs) are metastable planar defects that occur in all crystalline materials, depending on the synthesis route. They strongly influence mechanical properties [1–5], diffusion [3, 6–8], electrical conductivity [9–13], thermal conductivity [14–18], and others. It has been established theoretically [19–26] that GBs can occur in different GB phases [27], also called complexions [28–31], or more generally defect phases [32–34]. A thermodynamic treatment of these metastable GB phases as defects of stable bulk phases is possible by presupposing the existence of the GB. The GB phase with the lowest excess free energy is then the (meta-)stable interface phase at the given thermodynamic conditions. Recently, the formalism has been extended to the hypothetical case of a stable interface phase with zero excess free energy [35]. Analogous to bulk phases, GB phase transitions can be due to changes of composition [31, 36–40], but they can even exist in single-element materials, where just the GB structure changes [41–55].

GB phases are important, because they affect how the GB impacts the macroscopic material properties. This is true even in single-element systems, where for example GB mobility [56, 57] or diffusion [7, 8] are affected by GB phases.

GBs are characterized by five macroscopic parameters, covering the misorientation axis and angle θ between the abutting crystallites and the crystallographic planes that terminate on both sides of the GB [3, 4]. Here, we cover single-element systems with high-angle tilt GBs, where the rotation axis between the grains lies within the GB plane. Often, GBs with crystallographically equivalent planes on both sides of the GB are called symmetric. Finer distinctions exist, where GBs that are mirror planes are called symmetric and those with only equivalent planes, but no mirror symmetry, are called quasi-symmetric [58]. We will generally use the term “symmetric” to refer to both the quasi-symmetric and the symmetric case for simplicity. Most studies of GB thermodynamics have exclusively considered special GBs, such as symmetric GBs [43–49, 52–54], which typically have the lowest energy. However, tilt GBs found in real materials are never perfect and deviate from the ideal case by having a twist component or they are inclined by an angle ϕ from the nearest symmetric GB plane (asymmetric tilt GBs). GB phase transitions without segregation in these common cases are less well studied, al-

*Corresponding author

Email addresses: dehm@mpi-susmat.de (Gerhard Dehm), t.brink@mpi-susmat.de (Tobias Brink)

¹Present address: Interdisciplinary Centre for Advanced Materials Simulation (ICAMS), Materials Informatics and Data Science, Ruhr-Universität Bochum, Universitätsstr. 150, 44801 Bochum, Germany

though similar GB phases have been observed in symmetric and asymmetric GBs of pure Cu [50, 51].

There are two ways that the atomic structures can accommodate an inclination away from the symmetric plane. First, the GB can facet into the two nearest symmetric facets, increasing its area A , but potentially decreasing its overall excess free energy γ [59–71]. Alternatively, defects with step character can lead to inclination [61, 65, 71–76]. Apart from pure steps, common line defects in GBs are disconnections, which are characterized by a mode (**b**, h) [5]. The mode is a specific combination of the dislocation character (Burgers vector \mathbf{b}) of the defect and a corresponding step height h . Disconnections are responsible for GB plasticity in the form of shear-coupled motion [5] and can also influence macroscopic properties, such as diffusion [77, 78]. In terms of deviations from special GBs, the **b** component can change the twist and tilt misorientation and the h component can influence the inclination of the GB. Depending on the mode, disconnections can have different core and elastic energies [5]. The core energies, in turn, depend on the GB phase [57]. Thus, we expect that geometrically necessary disconnections and steps in asymmetric tilt GBs also influence the thermodynamic stability of the GB phases.

Here, we study asymmetric $\Sigma37c$ $[11\bar{1}]$ tilt GBs in Cu, because their symmetric variant exhibits a GB phase transition between two experimentally-observed GB phases with changing temperature [51]. We investigated the GBs using exhaustive structure search, molecular dynamics (MD) simulations, and scanning transmission electron microscopy (STEM) of Cu and Al samples. Our goal is to determine how the inclination affects the atomic structure and how defects and faceting in turn affect the thermodynamics of the GB phases.

2. Bicrystallography

First, we will revisit the previously-studied GB phases and crystallography (Fig. 1). The $\{1\ 10\ 11\}$ -type GBs (repeated every 60° due to the trifold symmetry along $[11\bar{1}]$) are quasi-symmetric GBs in the nomenclature of Ref. [58], in that they exhibit equivalent crystallographic planes on both sides of the GB, but the abutting crystallites are not mirrors of each other and are instead connected by another symmetry operation [58]. We arbitrarily define this plane as having inclination $\phi = 0^\circ$. This plane can have two types of GB phases, namely the “domino” (Fig. 1(d)) and the “pearl” (Fig. 1(e)–(f)) GB phase [51]. The pearl phase has two microstates with slightly different structures and energies. The domino structure is stable at low temperatures, while the pearl phase is stable at higher temperatures. The GB phases can transform into each other without requiring diffusion [51]. At $\phi = 30^\circ$, we find the symmetric $\{347\}$ GB planes. These GB planes are truly symmetric mirror planes and exhibit only the zipper GB phase [79, 80] (Fig. 1(b)). We will from now on no longer make the distinction between quasi-symmetric and symmetric GBs, and call

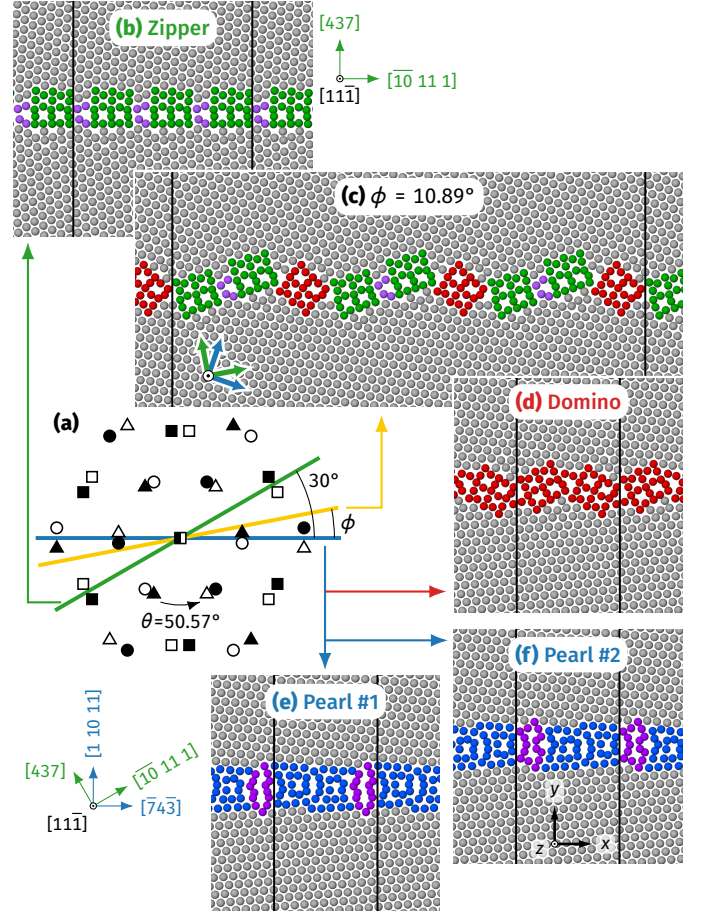


Figure 1: Bicrystallography of $\Sigma37c$ $[11\bar{1}]$ tilt GBs in Cu. (a) Part of the dichromatic pattern. The blue line represents the quasi-symmetric $\{1\ 10\ 11\}$ GB planes, while the green line represents the symmetric $\{347\}$ GB planes. Asymmetric GBs, with inclinations ϕ between these two cases are the subject of the present study (yellow line). The coordinate system in the bottom left represents the corresponding crystal directions in the upper crystallite. (b) The zipper GB phase at $\phi = 30^\circ$ depicted with the crystal orientations as indicated by the coordinate axes to the right of the image. The vertical black lines represent the periodic unit cell of the GB structure. (c) An asymmetric GB at intermediate $0^\circ < \phi < 30^\circ$ obtained as a mix of zipper (b) and domino (d) structures. (d)–(f) The domino and pearl phases on the $\{1\ 10\ 11\}$ GB planes. Note the difference in the purple structure for pearl #1 and #2. An asymmetric pearl phase is not depicted and will be studied in this work.

both symmetric for simplicity. A noteworthy feature of the domino phase is that it can also be regarded as consisting of nanoscaled facets of the zipper structure, which are driven energetically to their minimal length [81]. This allows the easy construction of asymmetric domino/zipper GBs by simply elongating one facet of the domino structure as shown in Fig. 1(c). We will therefore call the set of domino, zipper, and corresponding asymmetric GB phases simply the domino/zipper phase. The asymmetric pearl phase and the relative thermodynamic stability of these asymmetric GB phases have not been studied, yet, and are therefore the topic of the present work.

3. Methods

3.1. General simulation parameters

To model Cu, we used the Mishin et al. embedded atom method (EAM) potential [82] with the simulation code LAMMPS [83, 84]. For later use, we determined the lattice constant at $T = 0$ with this potential as

$$a = 3.615 \text{ \AA} \quad (1)$$

and calculated the values at a range of finite temperatures using the protocol described in Ref. [85].

3.2. Asymmetric grain boundary structures and structure search

We employed different strategies to find asymmetric GB structures in the present work. As a convention, we oriented the GBs in our simulations and (experimental) images such that the z direction coincides with the $[11\bar{1}]$ tilt axis and the y direction is the GB normal. The x direction is then the orthogonal direction within the GB plane. Sometimes, where noted, the x and y directions instead correspond to the closest symmetric GB plane.

First, we constructed a range of domino/zipper asymmetric GBs by starting from the domino structure and increasingly elongating one of the nanofacets [81], see also Fig. 1(c). For the bordering symmetric cases we used the following crystal directions for the upper (“top”) and lower (“bot”) crystallite:

$$\mathbf{x}_{0^\circ}^{\text{top}} = [\bar{7}4\bar{3}] \quad \mathbf{y}_{0^\circ}^{\text{top}} = [1\ 10\ 11] \quad \mathbf{z} = [11\bar{1}] \quad (2)$$

$$\mathbf{x}_{0^\circ}^{\text{bot}} = [\bar{4}73] \quad \mathbf{y}_{0^\circ}^{\text{bot}} = [10\ 1\ 11] \quad (3)$$

$$\mathbf{x}_{30^\circ}^{\text{top}} = [\bar{10}\ 11\ 1] \quad \mathbf{y}_{30^\circ}^{\text{top}} = [437] \quad (4)$$

$$\mathbf{x}_{30^\circ}^{\text{bot}} = [\bar{1}\ 11\ 10] \quad \mathbf{y}_{30^\circ}^{\text{bot}} = [7\bar{3}4]. \quad (5)$$

The construction by elongation of a nanofacet and subsequent rotation yielded various asymmetric GBs that are periodic in x and z direction.

Using the resulting crystal directions and periodicities, we also performed an exhaustive structure search with the software GRIP [54]. This code searches for GB structures not only by varying relative displacements between the upper and lower crystal (γ -surface method) and running short MD simulations, but also by adding or removing atoms in the GB region, yielding GB structures that cannot be found with a constant number of atoms [43, 44, 46, 54]. Due to the large size of the periodic cell of the asymmetric GBs, we did not run the search for any supercells, but only the smallest possible sizes in the periodic x and z directions.

For all structures, we fixed the lattice constant to its zero-temperature value a , so that the GBs were constrained in x and z directions by the bulk material, only allowing volume relaxation normal to the GB [24, 25]. We therewith obtained the ground-state GB energy

$$\gamma_0 = [E_{\text{pot}}], \quad (6)$$

where E_{pot} is the system’s potential energy at $T = 0$ and the square brackets mark the excess of any extensive property Z [21, 25], defined as

$$[Z] = \frac{Z_{\text{GB}} - \frac{N_{\text{GB}}}{N_{\text{bulk}}} Z_{\text{bulk}}}{A}. \quad (7)$$

Here, Z_{GB} is calculated in a region containing a GB with area A and N_{GB} atoms, while the reference state is a defect free crystal region with the property Z_{bulk} for N_{bulk} atoms.

3.3. Annealing with molecular dynamics

Additionally, we performed MD simulations to anneal samples at various temperatures in order to determine their equilibrium GB phases. For these simulations we used a time integration step of 2 fs and a Nosé–Hoover thermostat at the desired temperature T . We again employed periodic boundary conditions in x and z direction, as well as open boundaries in y direction. In the periodic directions, the size of the simulation cell was set in accordance with the finite-temperature lattice constant of the bulk material. In x direction, the various symmetric and asymmetric GBs had different periodic lengths. In order to keep the simulations of roughly comparable size (on the order of 150 000 to 170 000 atoms), we repeated the periodic segments as necessary to reach sizes between 700 Å and 800 Å. In the open y direction, we kept a size of 400 Å to minimize interaction of the GBs’ stress fields with the surface. In z direction, along the tilt axis, we only used a single unit cell with length $a\sqrt{3} \approx 6.3$ Å. While this also minimizes the required computational power, we mainly chose this value to accelerate the kinetics of the GB phase transition at temperatures close to room temperature. It was shown before that the GB phase junction between two GB phases moves slower the larger the system size along the tilt axis [50]. The periodic lengths were scaled and fixed in accordance with the bulk material’s lattice constant at the given temperature T . Annealing simulations were then performed for 100 ns. Subsequently, the structures were rescaled to the zero-temperature lattice constant a and minimized to extract the ground-state GB energy γ_0 for comparison with the results of the structure search.

3.4. Quasi-harmonic approximation

The stability of the GB phases at finite temperatures is defined by the excess free energy

$$\gamma = [G] = [U] - T[S] \quad (8)$$

at zero externally applied stress [25]. While the excess internal energy $[U]$ can be obtained directly from MD simulations, the excess entropy $[S]$ requires other methods.

Here, we use the quasi-harmonic approximation (QHA) for the vibrational part of the free energy [86, 87]. For this, we computed the force constant matrix with the `dynamical_matrix` command in LAMMPS, which was diagonalized to obtain the eigenfrequencies ν_i . We considered

only a classical approximation for the excess free energy since (i) we previously found the difference to the quantum mechanical approximation to be minor above 50 K [51, 55] and (ii) we compare the results to classical MD simulations. The free energy of a system is thus calculated as

$$F(T) = E_{\text{pot}}(T) + k_B T \sum_{i=1}^{3N-3} \ln \frac{h\nu_i}{k_B T} \quad (9)$$

and G is obtained by calculating F at the equilibrium lattice constant at each temperature [86, 87].

For asymmetric GBs, the computation of the excess properties from the QHA data is more complex. The free energy from the QHA must always be calculated for the whole system [51] and thus requires the subtraction of the surface energies Γ , which differ for the upper crystal (Γ_{top}) and lower crystal (Γ_{bot}). For each GB, we thus computed the free energies for three slabs with open surfaces in y direction and periodic boundaries in x and z : G_{GB} for a slab with a GB, as well as G_{top} and G_{bot} for defect-free slabs corresponding to the orientation and surfaces of the upper and lower crystallite. Additionally, we calculated G_{fcc} for a fully periodic, defect-free fcc crystal. Thus, we compute

$$\Gamma_{\text{top}} = \frac{G_{\text{top}} - N_{\text{top}} \frac{G_{\text{fcc}}}{N_{\text{fcc}}}}{2A} \quad (10)$$

$$\Gamma_{\text{bot}} = \frac{G_{\text{bot}} - N_{\text{bot}} \frac{G_{\text{fcc}}}{N_{\text{fcc}}}}{2A} \quad (11)$$

$$\gamma = \frac{G_{\text{GB}} - N_{\text{GB}} \frac{G_{\text{fcc}}}{N_{\text{fcc}}}}{A} - \Gamma_{\text{top}} - \Gamma_{\text{bot}}, \quad (12)$$

where the GB area A is equal to the surface area on one side of the slab due to our construction of the simulation cells. Alternatively, we can also write

$$\gamma = \frac{G_{\text{GB}} - \frac{G_{\text{top}}}{2} - \frac{G_{\text{bot}}}{2}}{A} \quad (13)$$

if $N_{\text{GB}} = N_{\text{top}} = N_{\text{bot}}$. This is useful to determine if the system containing the GB is big enough to avoid interactions between surface and GB. If the system is too small, the error can be estimated by the discrepancy between Eqs. 12 and 13.

3.5. Experimental methods

We additionally investigated several asymmetric GBs experimentally with STEM. For this, we used Cu and Al samples, to be able to compare the results of two different fcc metals. In order to obtain high-resolution atomic images of tilt GBs, $\{111\}$ -textured films are required. The recipe and details of the growth of Cu thin films with a $\{111\}$ surface orientation can be found in Refs. [51, 79], as the same thin film was used for the present experiments. Similarly, $\{111\}$ -textured Al thin films were deposited following the procedure described in Ref. [76]. The resulting films in both

Cu and Al possess grains with sizes of tens of micrometers with a sharp $\{111\}$ texture separated by $\langle 111 \rangle$ tilt GBs.

For selecting and identifying $\Sigma 37c$ GBs in Cu, the film was scanned with a Thermo Fisher Scientific Scios2HiVac dual-beam secondary electron microscope (SEM) equipped with an electron-backscattered diffraction (EBSD) detector. The focused Ga^+ ion beam (FIB) of the dual-beam SEM was used to lift out the GBs of interest. Thinning of the lamellae was performed with ion beam voltage and current being gradually reduced from their starting values of 30 kV and 0.1 nA down to 5 kV and 16 pA.

For Al, the thin films were analyzed by EBSD at 20 kV using a JEOL JSM-6490 SEM. Given that Ga implantation can lead to embrittlement in GBs [88], a Xe-based plasma FIB (PFIB) milling process was employed for the preparation of the Al lamellae. The PFIB milling was carried out using a Helios G3 Cx dual-beam SEM/FIB system (Thermo Fisher Scientific) and the parameters applied for plan-view STEM sample preparation are detailed in Ref. [76].

All samples were subsequently analyzed in a probe-corrected FEI Titan Themis 80-300 (Thermo Fisher Scientific). A high-brightness field emission gun at a voltage of 300 kV and currents of 70 to 80 pA were used to scan the area of interest. The STEM images were recorded with a high-angle annular dark-field (HAADF) detector (Fishione Instruments Model 3000) with collection angles of 78 to 200 mrad and a semiconvergence angle of 17 mrad. The images shown in this study are averaged over 50 to 100 frames and filtered with a background subtraction filter, Butterworth filter, and Gaussian filter to reveal the atomic structures of the GBs, ensuring that the structures of the original image were not modified by using the applied filters.

3.6. Determination of Burgers vectors

We first analyze line defects in our GBs in terms of their Burgers vector. The Burgers vector of a disconnection is defined as the dislocation content of the defect without the intrinsic dislocation content of the GB (according to, e.g., Read–Shockley [89]). For this, half Burgers circuits are drawn in both crystallites along low-index crystal directions, rotated into a common coordinate system, and then summed [90]. The issue is that this circuit cannot be reliably drawn in the GB core. However, the GB structure on both sides of a disconnection is the same, so we can choose two equivalent GB crossings across the same GB motifs that cancel each other [69] (see also Refs. [57, 76, 81] for more examples). We always draw the circuit counter-clockwise around the z axis for consistency. This allows us to correctly evaluate the net defect content of edge dislocations that fully span the length of the GB along the tilt axis direction.

There are some cases, where this is not possible. One example would be the GB phase junction, which is the line defect separating two GB phases, where the GB crossings are necessarily different on each side of the defect [91]. Here, we can instead directly measure lines crossing a GB segment

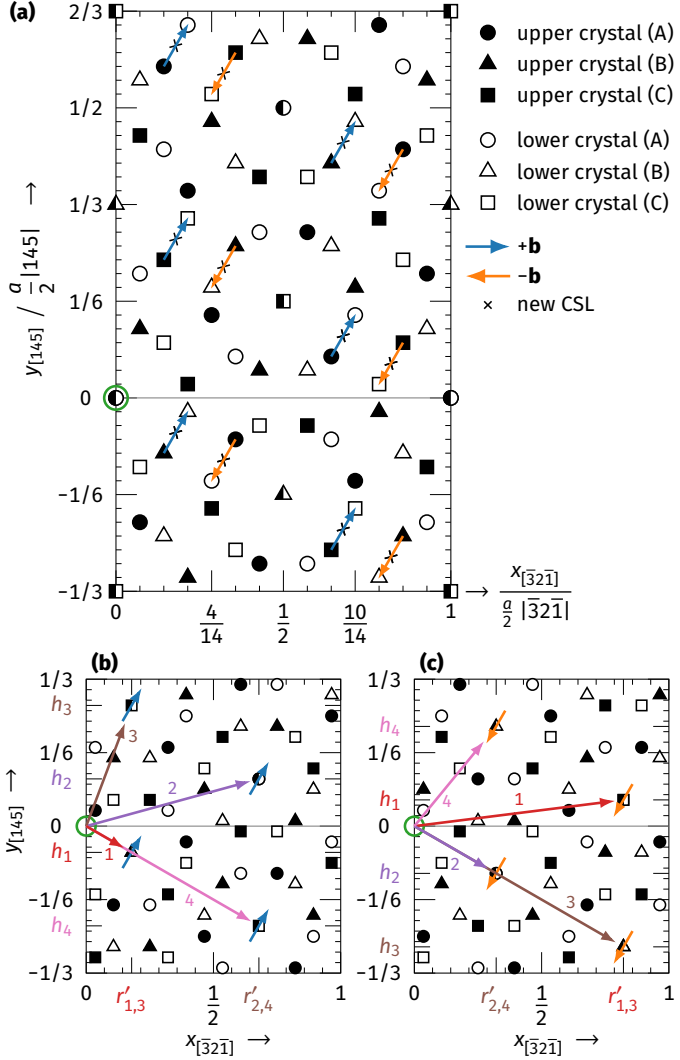


Figure 2: Obtaining disconnection properties from a dichromatic pattern, here exemplarily for $\Sigma 7$ [11̄] tilt GBs (a). Blue and orange arrows show two possible DSC vectors $\pm\mathbf{b}$. Applying $+\mathbf{b}/2$ or $-\mathbf{b}/2$ displacements to the crystallites, yields the new patterns in (b) and (c), respectively. New coincidence sites lie halfway along the arrows indicated in (a). The arrows numbered 1–4 in (b) and (c) show the distance from the old to the new coincidence sites. Each number corresponds to a different type of defect, whose step height is the component of the arrow normal to the GB plane.

in a defect-free reference structure corresponding to that segment. The translation into the reference structure uses atomic motifs as orientation points [91].

The GB phases and their defects were analyzed and visualized with OVITO [92]. We did not employ the automated Interfacial Line Defect Analysis (ILDA) method [93], because it currently requires the clear identification of an atom within the GB as a coincidence site. Due to the complex reconstructions of domino/zipper and pearl, it was not possible to correctly define these sites. We therefore analyzed the defects manually as described above.

3.7. Defect mode analysis

For a given Burgers vector \mathbf{b} , the dichromatic pattern yields additional information about the disconnection mode. To demonstrate this, Fig. 2 shows a $\Sigma 7$ [11̄] tilt GB with a simpler dichromatic pattern than our $\Sigma 37c$ GBs. The dichromatic pattern is simply the overlay of the atomic coordinates of the upper and lower crystallite, such that certain atoms of both crystallites occupy the same position (coincidence sites) [94]. The coincidence sites form the coincidence site lattice (CSL), which is periodic. The possible Burgers vectors can then be drawn to connect two sites in the dichromatic pattern, forming the displacement-shift-complete (DSC) lattice [3, 5, 94]. We can (arbitrarily) imagine the left side of the defect corresponding to the pattern in Fig. 2(a), while the right side of the defect corresponds to a pattern that was obtained by a relative shift \mathbf{b} between the crystallites (Fig. 2(b)). To minimize overall strain in the system, we apply a displacement of $\mathbf{b}/2$ to the upper crystallite and $-\mathbf{b}/2$ to the lower crystallite. A new coincidence site can thus be found in Fig. 2(a) halfway along the Burgers vector, marked by an x. We could measure every interesting property using this point, but also illustrate the shifted dichromatic patterns in addition. We see that the dichromatic pattern is equivalent, but underwent a translation. This is the (common) case when \mathbf{b} is not a CSL vector.

The step height h of a disconnection can be measured as the offset normal to the GB between two crystallographically equivalent sites on both sides of the defect. Since this offset will be the same for any site, we choose a coincidence site for simplicity. The green circle in Fig. 2 corresponds to the “left” coincidence site. Obviously, for a given \mathbf{b} , an infinite number of possible new equivalent sites exist (Fig. 2(b)) and thus an infinite number of possible step heights. Steps that have a component along the tilt axis (z) are also possible: Defect 1 in Fig. 2(b) connects a coincidence site on stacking plane A with one on plane B. These defects introduce an additional z step into the atomic structure of the GB, but do not influence the GB plane, unlike the step h . Smaller step heights are likely energetically favorable [95, 96], although sometimes, e.g., the second smallest step can be preferred [57]. We note that inverting the Burgers vector also inverts the step heights (Fig. 2(c)), which we will discuss in more detail in the results.

We are also interested in the minimum distance r between two disconnections. If two defects do not overlap, we must find an equivalent site on each side of the defect that is not part of the next defect’s core. These equivalent sites are found in defect-free structures with the periodicity R of the CSL. However, when the dichromatic pattern is shifted, an additional distance r' must be considered (marked in Fig. 2(b)–(c) on the abscissa). The exact minimum distance r depends on the atomic structure of the defect, but the admissible values are $r = |nR \pm r'|$, with n being an integer.

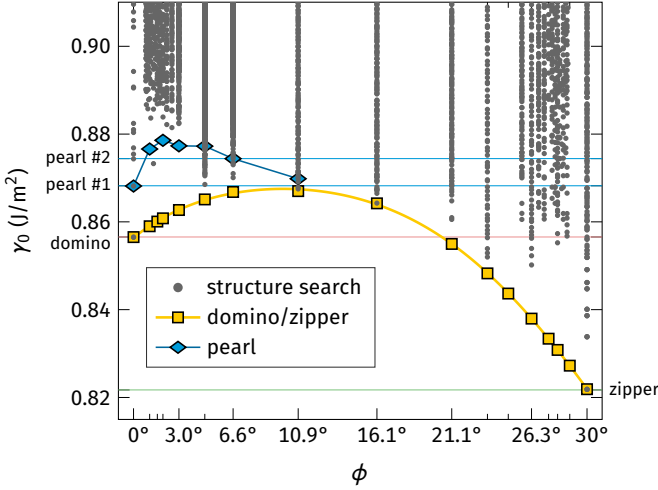


Figure 3: Ground state energies γ_0 of GBs found via structure search, construction of low-energy domino/zipper GBs, or by annealing simulations. The data is presented as a function of the GB inclination ϕ from the symmetric reference plane (1 10 11). The second symmetric plane, (437), is located at $\phi = 30^\circ$. The energies of the symmetric GB phases are indicated with horizontal lines.

4. Grain boundary phases as a function of inclination

4.1. Structure search

We used different strategies to search for possible GB phases with inclinations from 0° to 30° . First, we constructed domino/zipper GBs by starting from the domino structure and continually increasing one facet [81]. This yields periodic simulation cells with a range of finite inclinations. Using the crystallographic planes obtained with this method, we also started a structure search with GRIP for the same inclinations. These calculations each yield dozens to hundreds of GB structures, many of them defective. Figure 3 shows the resulting GB energies γ_0 of the ground state. For small inclinations the periodic cell length is comparatively large and GRIP cannot easily find low-energy structures. For the symmetric GBs and $\phi = 6.59^\circ, 10.89^\circ$, however, GRIP yields good results. It still finds mostly reasonable structures in the range $4.72^\circ \leq \phi \leq 23.41^\circ$. We find that the ground state GB energy of the domino/zipper phase is always the lowest one, although it cannot always be found with GRIP.

Additionally, we extracted the lowest-energy pure pearl structures. Non-faceted pearl phases only exist up to 10.89° . Beyond that, we find either the domino/zipper phase or a mix of zipper and pearl facets. For 1° to 3° , the GRIP structures have relatively high GB energies, and we found lower-energy pearl structures by following an annealing procedure. In that case, we annealed a starting domino/zipper structure for 100 ns at 400 K and then minimized the result. Consequently, the pearl data points in Fig. 3 for low ϕ come from the annealing simulations.

It stands to reason that the constructed domino/zipper GBs are the overall lowest-energy structures. Neither struc-

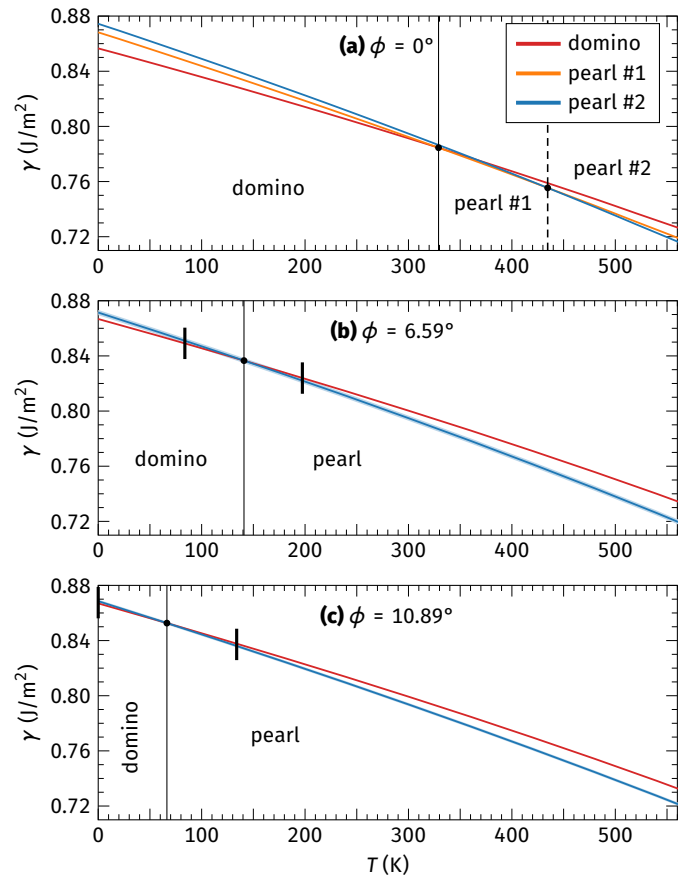


Figure 4: Excess free energy calculations for pearl and domino GB phases at some representative inclinations ϕ . The predicted GB phase transitions and stability ranges are marked. For the asymmetric pearl GBs (blue lines in (b),(c)), different ways to subtract the surface free energy (see Eqs. 12 and 13) yield slightly different results. This is likely due to the limited simulation cell size, where strain fields of GB and surface slightly overlap. The estimated range of possible values is indicated by the blue shaded areas. The vertical marks represent the resulting uncertainty of the transition temperature.

ture search with GRIP, nor annealing yielded lower-energy structures in any case. For the pearl phase, the structures we found have GB energies very close to the symmetric pearl phase. We will discuss the structures and their defects in detail in Sec. 5 and first focus on the stability of these GB phases as a function of temperature.

4.2. Excess free energy

Free energy calculations with the QHA are only possible for smaller simulation cells, since the eigenfrequency calculations require large amounts of memory and CPU time. Thus, we compared domino and pearl phases for $\phi = 0^\circ, 6.59^\circ$, and 10.89° , where low-energy structures with small periodic lengths along y could be obtained with GRIP. Figure 4 shows the results.² Similar to the GB energies at

²Some of us reported a higher transition temperature of 460 K for the symmetric case in an earlier work [51]. In a later work [53] and in the present case, we used a bigger cell for the free energy

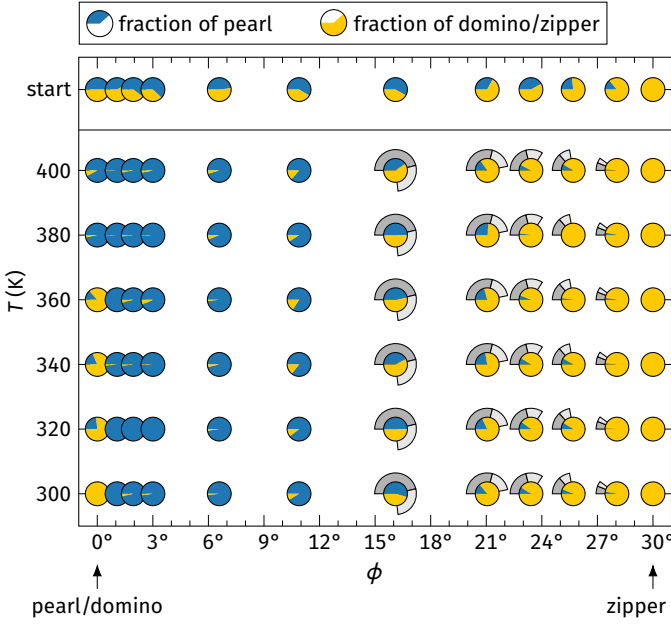


Figure 5: The GB phases present in asymmetric tilt GBs after equilibrating at temperatures between 300 K and 400 K for $t = 100$ ns. The topmost row shows the fraction of GB phases in the starting structure, which were structures obtained with GRIP that contain both pearl and domino/zipper. For $\phi = 0^\circ$, we constructed a box with one big region each for pearl and domino. Results with additional starting structures are provided in Supplemental Fig. S1. For each inclination and temperature, the pie chart shows the fraction of the two GB phases. Starting from 16° , there are gray bars around the data points. These indicate the maximum possible fractions of pearl phase in faceted GBs (see Sec. 5.3). The dark gray region is for symmetric pearl facets. The light gray region indicates how much longer the pearl facets can become if they are asymmetric ($\phi = 10.89^\circ$).

0 K (Fig. 3), the excess free energy of the pearl phases is only slightly higher for the asymmetric GBs than for the symmetric GB. The domino phase, however, exhibits a steadily increasing excess free energy with higher inclinations ϕ . As a consequence, the simulations predict that the domino phase is only stable at very low temperatures in asymmetric GBs. A reasonable hypothesis is that domino and pearl exhibit different kind of defects with different energies in asymmetric GBs. We will analyze these defects in detail later in Sec. 5.

4.3. Annealing simulations

In order to check the QHA results over a larger range of inclinations, we performed several annealing simulations. First, we selected defective GRIP structures that contained both domino and pearl. For each inclination, we chose two different cells and annealed each structure for 100 ns at a range of temperatures (Fig. 5 and Supplemental Fig. S1(a)). We also started from the pure domino/zipper phase (Supplemental Fig. S1(b)). Finally, we used the outcome of

calculations and obtain 330 K instead. This highlights the sensitivity of these results to small numerical errors due to the very similar slope of the free energy curves. We will discuss the match to annealing simulations and experiment further down.

these simulations at 400 K that contained a large amount of pearl, for which we restarted the annealing process at different temperatures (Supplemental Fig. S1(c)).

The results for $\phi \leq 10.89^\circ$ mostly follow the predictions from the QHA calculations. Domino is only stable in this temperature range for $\phi = 0^\circ$. In these symmetric GBs, domino transforms into pearl above 340 to 360 K, close to our prediction using the QHA. Below that temperature range, the results depend on the starting condition due to the slow kinetics and mixed structures can occur. Nevertheless, pure pearl GBs start transforming into domino (Supplemental Fig. S1(c)), which indicates that the QHA calculations (Fig. 4) correctly predict the transition temperature. The fact that we often obtain metastable mixed structures highlights the small free energy differences of the GB phases in this temperature range. When starting from a pure domino structure in asymmetric GBs, the domino phase remains in the system at low temperatures (Supplemental Fig. S1(b)). This evidences the relatively slow kinetics of GB phase transitions and the resulting hysteresis of the transition. The simulations starting from mixed pearl/domino phase are more revealing: the domino phase disappears for $0^\circ < \phi \leq 10.89^\circ$ (Fig. 5). We conclude that simulations initially containing a mix of domino/zipper and pearl phases very likely contain equilibrated GBs, because we can clearly observe changes of the GB phase fractions and do not require nucleation. This is aided by the thin size (6.3 Å) in the periodic z direction, which minimizes the barriers for the movement of line defects. We also tried temperatures below 300 K, but we no longer observed any significant structural changes within the simulation timeframe and therefore excluded these simulations.

Above 10.89° , GBs contain both pearl facets, as well as domino/zipper facets. This indicates that the stabilization of pearl is no longer favorable compared to faceting. To understand this behavior, we need to analyze the defects responsible for the inclination.

5. Analysis of the grain boundary defects

5.1. Low inclination angles

In order to understand the change of stability, we systematically looked at the GB structures we obtained and analyzed the type of defects present in the GBs. Contrary to symmetric GBs, asymmetric GBs are composed of pre-existing defects to compensate the deviation of the inclination angle. Figure 6 shows an illustration of the possible defects that lead to asymmetric inclinations without faceting. Either pure steps or disconnections (consisting of a Burgers vector plus a step) are found. The total inclination is a result of the sum of step heights h and the distance r between defects:

$$\tan \phi = \frac{\sum_i h_i}{\sum_i r_i}. \quad (14)$$

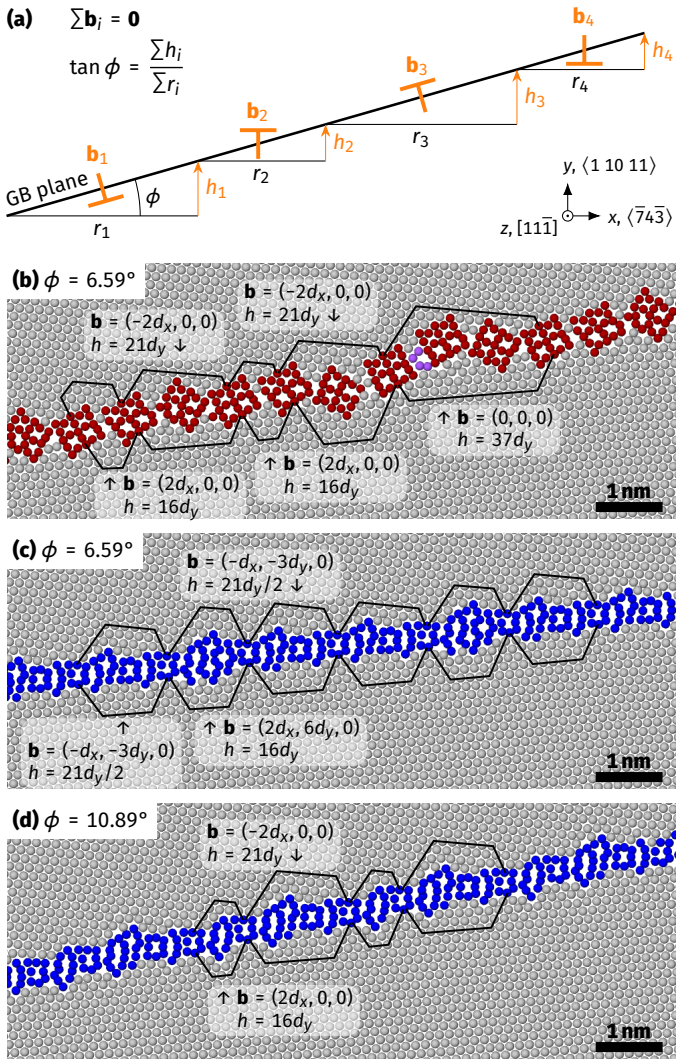


Figure 6: Compensation of the inclination at the atomic scale by disconnections and steps. (a) Schematic of different disconnection modes (consisting of Burgers vector \mathbf{b} and step height h) with different slip systems present in asymmetric GBs. (b) Domino structure from an annealing simulation at 300 K. It contains disconnections in addition to pure steps. (c)–(d) Low-energy pearl structures from GRIP. The indicated disconnections repeat periodically to achieve the inclination. Note that in all cases the Burgers vectors add up to zero on short length scales to minimize energy and to preserve the misorientation.

In order to preserve the misorientation between the crystallites, we require that

$$\sum_i \mathbf{b}_i = \mathbf{0}, \quad (15)$$

summing over all defects with Burgers vectors \mathbf{b} in the GB. Otherwise, the misorientation between the abutting grains would change [97, 98] (cf. the Frank–Bilby equation [99, 100]). We note already from Fig. 6 that the total Burgers vector seems to be compensated by alternating different disconnection modes (\mathbf{b}, h).

We investigated our asymmetric tilt GBs at different temperatures and inclination angles and compiled a list of the disconnection types observed in each GB phase. Figure 7

shows the observed Burgers vectors in the dichromatic pattern. We also measured the dislocation spacing r along the GB plane by choosing the two closest equivalent sites left and right of the disconnection core and measuring their projected distance along the symmetric GB's x direction. We compared this with the admissible spacings from the dichromatic pattern (see methods in Sec. 3.7).

We categorize the disconnection types by their mode (\mathbf{b}, h) , see Fig. 7. Additionally, we differentiate between disconnections with a zero b_y component normal to the GB plane (glide disconnections) and disconnections with nonzero b_y component (climb disconnections). This is because the slip plane of the glide disconnection is equal to the GB plane and they are consequently mobile. The climb disconnections possess a slip plane that is not equivalent to the GB plane. Since disconnections cannot exist outside the GB, these disconnections require disconnection climb—and thus diffusion—to move along the GB [5, 101, 102]. Glide disconnections are generally found in symmetric GBs during shear-coupled GB migration [5, 103–105].

The GB disconnections observed in domino and pearl are shown in Figs. 8 and 9. We express the Burgers vectors and step heights in units of the lattice spacings (see also Fig. 7), which are

$$d_x = \frac{a}{2 \cdot |347|} \approx 0.21 \text{ \AA} \quad (16)$$

$$d_y = \frac{a}{2 \cdot |10\bar{1}1|} \approx 0.12 \text{ \AA} \quad (17)$$

$$d_z = \frac{a}{|111|} \approx 2.09 \text{ \AA}, \quad (18)$$

where $|hkl|$ is the length (L_2 -norm) of the vector (h, k, l) . Generally, the disconnection types I, II, III, and IV are the most commonly observed ones. They have the shortest Burgers vector (0.42 \AA) and thus also a low defect energy.

Table 1: Comparison of inclinations obtained by representative combinations of disconnections that lead to an overall Burgers vector of zero, but a nonzero overall step height h . Type S is a pure step; see Fig. 7 for the other individual disconnection types. There is a minimum possible spacing r_{combined} between one combined defect and the next, similar one. It is used to calculate the maximum inclination $\phi_{\text{max}} = \arctan(h/r_{\text{combined}})$. Note that $d_y/d_x = 1/\sqrt{3}$.

Defect combination		h	r_{combined}	ϕ_{max}
Domino	S	$n \cdot 37d_y$	$(1 + n/2)74d_x$	0° – 30°
	I+II	$37d_y$	$111d_x$	10.89°
	III+IV	$37d_y$	$111d_x$	10.89°
	I+IV+V	$37d_y$	$132d_x$	9.19°
	II+III+V	$37d_y$	$185d_x$	6.59°
Pearl	I+II	$37d_y$	$111d_x$	10.89°
	III+IV	$37d_y$	$111d_x$	10.89°
	VI+VII	$37d_y$	$111d_x$	10.89°
	2×VII	$74d_y$	$116d_x$	20.22°
	2×III+VIII	$37d_y$	$185d_x$	6.59°
Zipper	S	$n \cdot 37d'_y$	$(1 + n/2)74d'_x$	0° – 30°

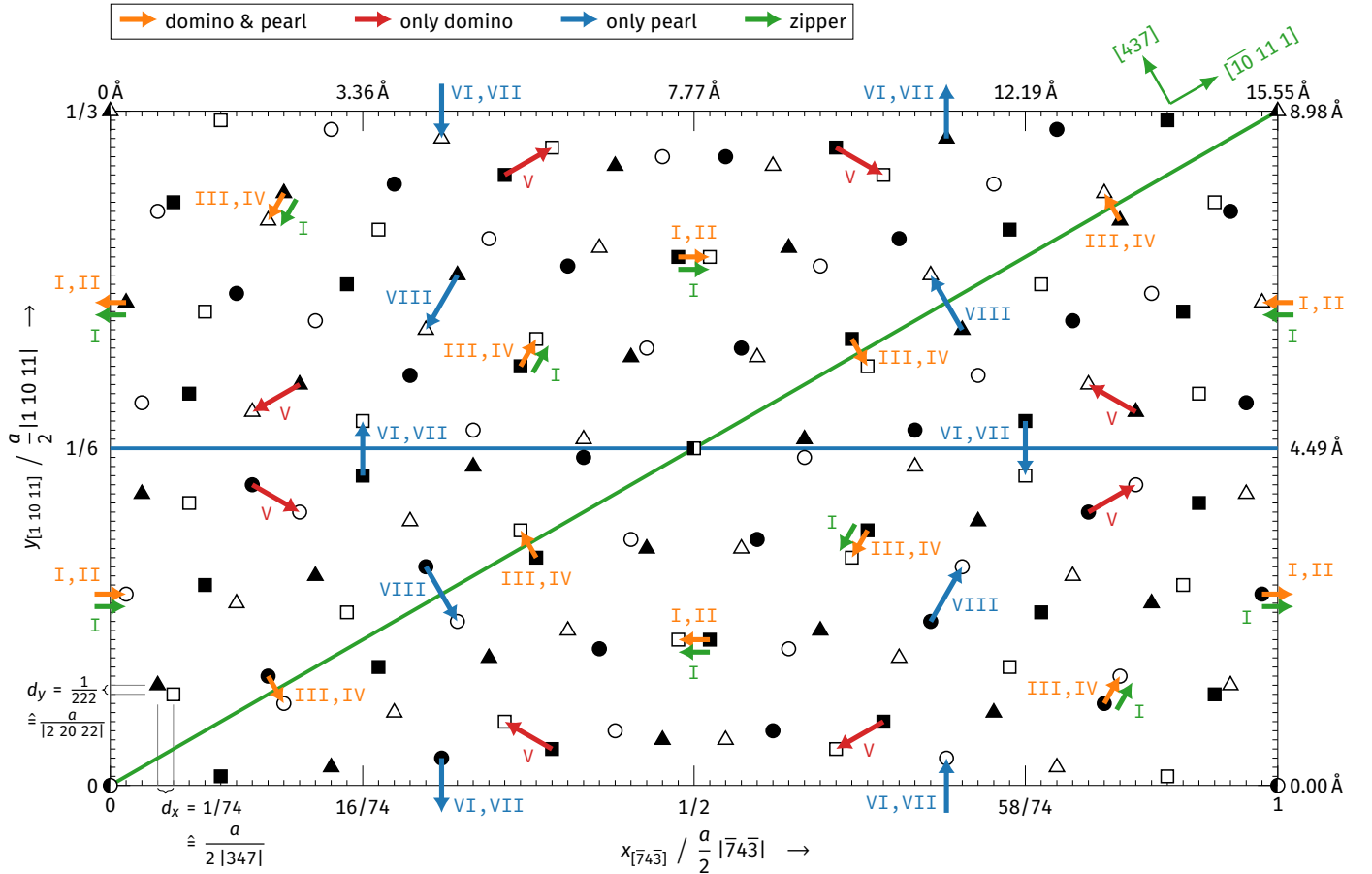


Figure 7: Part of the dichromatic pattern of $\Sigma 37c$ $[11\bar{1}]$ tilt GBs. The full pattern is shown in Supplemental Fig. S2. Arrows indicate the Burgers vectors of the observed disconnections. The horizontal blue line schematically indicates the GB plane of the pearl and domino GB phases, the inclined green line indicates the plane of the zipper GB phase. The ticks on both axes represent the lattice spacings d_x and d_y . The fractions on the left and bottom axes refer to the periodic lengths of the CSL lattice.

Types I/II and III/IV differ by their orientation towards the GB plane, with I and II being glide disconnections and III/IV being climb disconnections. As discussed earlier, domino can also have pure steps, here named type S.

Our analysis shows that the sign of the step height h is dependent on the Burgers vector component b_x (see Supplemental, Sec. III). This means that when a single disconnection type (\mathbf{b}_1, h_1) is used, no total step height can be achieved while conserving overall $\mathbf{b} = \mathbf{0}$, because $-\mathbf{b}_1$ leads to $-h_1$. Different modes, in contrast, can be summed up such that the overall Burgers vector is zero, but the overall step height is not: $(\mathbf{b}_1, h_1) + (\mathbf{b}_2, h_2) = (\mathbf{0}, h)$. We find that I and II can have the same sign of the step height when their Burgers vectors have opposite signs. Thus, they can compensate each others Burgers vector while leaving behind a step. These pairs are for example observed in Fig. 6 for domino and for pearl at $\phi = 10.89^\circ$. Type III and IV work the same way. At higher inclination angles and temperatures, defects with larger Burgers vectors are also observed. We found type V only in domino and types VI–VIII only in pearl. Interestingly, the combination of two times type III with one type VIII defect leads to a low-energy pearl structure at $\phi = 6.59^\circ$ (Fig. 6 shows the

structure obtained with GRIP).

A list of several defect combinations is provided in Table 1. It is not exhaustive, but contains representative low-energy configurations. Given the observed minimum distances r between individual defects (Figs. 8–10), we calculate the minimum distance r_{combined} between defect combinations as the sum of r . We can thereby estimate the maximum inclination change that can be achieved by these disconnection combinations as $\phi_{\text{max}} = \arctan(h/r_{\text{combined}})$. If the distance between defects is larger than r_{combined} , the inclination change is smaller. We see that typically the range of inclinations is limited to at most 11° , except for pure steps in domino. This fits to the earlier observations, where pure pearl structures were not found above $\phi = 10.89^\circ$, neither when annealing nor with the structure search method. Instead, faceted structures were found. There is one defect combination of two times type VII for pearl that could hypothetically achieve $\phi = 20.22^\circ$, but we did not observe this in our simulations, most likely due to the high defect energy.

To connect this to the relative stability, we can estimate the line energy of the defect combinations from $\gamma_0(\phi)$ (Fig. 3). For this, we project the GB energy onto the sym-

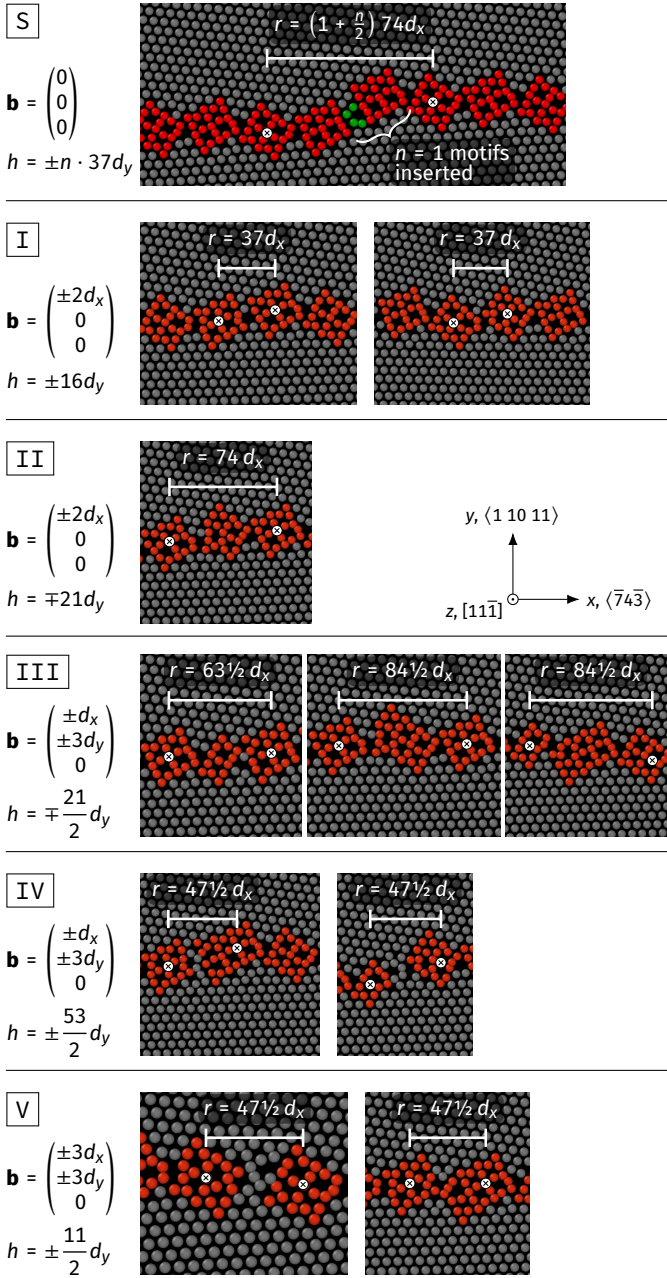


Figure 8: The disconnection types observed in asymmetric domino GBs. The sign of h depends on the sign of b_x (either the same or the opposite sign), while the sign of b_y is independent. The disconnection spacing r was measured as the projected distance along x between the two closest equivalent sites adjacent to the disconnection core (marked atoms).

metric GB plane and normalize by the defect distance r :

$$\frac{E_{\text{def}}}{t} = r \left(\frac{\gamma_0(\phi)}{\cos \phi} - \gamma_0(\phi=0) \right), \quad (19)$$

where E_{def} is the defect energy and t is the line length of the defect combination (i.e., the sample thickness). Using

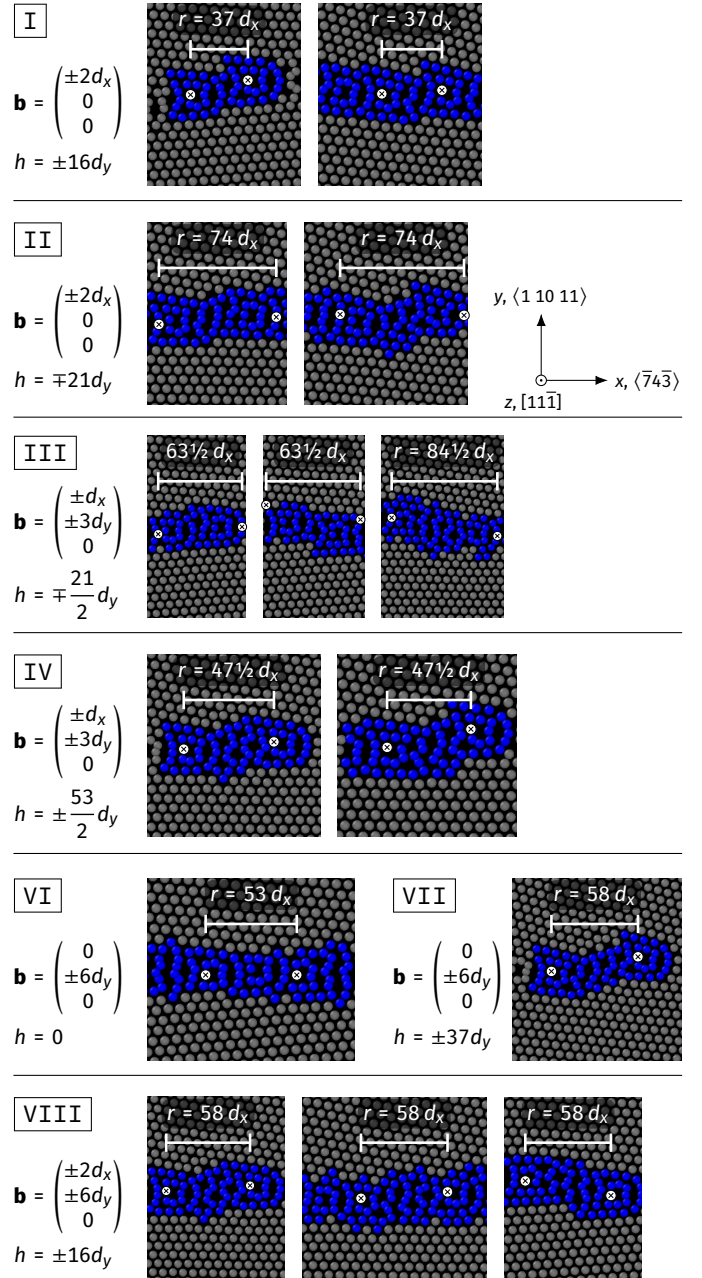


Figure 9: The GB disconnection types observed in pearl of $\Sigma 37c$ asymmetric grain boundaries. The signs of h depend on the sign of b_x (either same or opposite), while the sign of b_y is independent. This means that for type VII, both signs for the step are always possible.

the values in Table 1, we obtain

$$\begin{aligned} \text{domino: } & 62 \text{ pJ/m (S, } n = 1) \\ \text{pearl } 6.59^\circ: & 47 \text{ pJ/m (2×III+VIII)} \\ \text{pearl } 10.89^\circ: & 41 \text{ pJ/m (I+II)} \end{aligned}$$

(see Supplemental Fig. S3 for more details). The values for domino depend only very weakly on the inclination (changes < 2 pJ/m from 1° to 11°). For the same resulting step height ($37d_y$), the combined pearl defects cost less energy than the steps in domino, thereby stabilizing the

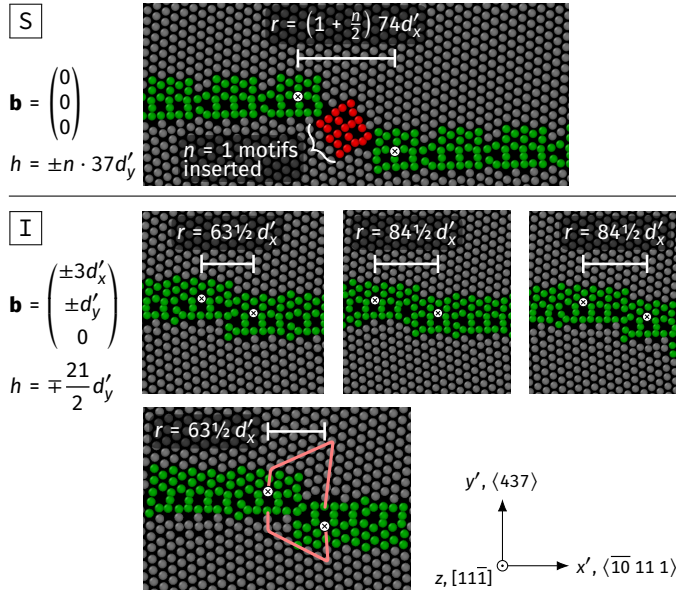


Figure 10: The step and disconnection observed in asymmetric zipper GBs. Values are expressed in the indicated coordinate system, which is aligned with the GB plane and therefore differs from Figs. 8–9. The sign of h depends on the sign of b_x (either same or opposite), while the sign of b_y is independent. The step S is equivalent to the steps in domino, only now rotated onto the zipper GB plane. In the last snapshot, the zipper motifs on the left and right of the defect are mirrored, so that the equivalent sites are once on top and once on the bottom of the square motif. This is expected, there are two degenerate states of the zipper structure that are sheared either to the left or right [81]. This additional shear must cancel out in the Burgers circuit (red lines). We verified that this is true also with the Frolov et al. method [91] for the Burgers circuit.

asymmetric pearl phases.

In some cases, phase junctions [91] between domino and pearl occur (Supplemental Fig. S4). They also have a Burgers vector [91]. For a pure phase junction without any adjacent disconnections, we find a Burgers vector of approximately $(0.20 \text{ \AA}, 0.08 \text{ \AA}, 0.62 \text{ \AA})$ in accordance with the values obtained in previous observations [51], see Supplemental Fig. S4. For $\phi \leq 11^\circ$, pearl and domino should not coexist in thermodynamic equilibrium. While GB phase patterning can exist, it is not possible in perfect $\Sigma 37c$ tilt GBs due to their high junction energies [106]. Experimentally observed patterning in this GB type is either due to additional defects to compensate a twist or tilt component, or due to the slow GB phase transition kinetics [50, 51]. Here, the phase junctions are thus not relevant for the stability of the GB phases in pure tilt boundaries. They are artifacts of the slow GB phase transition kinetics close to room temperature.

We also studied the disconnections in the zipper GB phase, which lies on the other symmetric GB plane (Fig. 10). We examined these defects in the coordinate system aligned with the GB plane and therefore express values in terms of the lattice spacings $d'_x = d_y$ and $d'_y = d_x$. Zipper structures contain fewer defects than the pearl and domino structures and we only found disconnections of type I, which is a

climb defect. Glide defects in zipper would have much larger Burgers vectors (cf. Fig. 7) and do not seem to occur here. We note that combinations of the observed disconnection cannot both lead to $\mathbf{b} = \mathbf{0}$ and $h \neq 0$, so inclination changes are solely due to pure steps. These steps are the same as for domino.

5.2. Experimental evidence

HAADF-STEM images of several asymmetric GBs in Cu are shown in Fig. 11. We first note that a significant amount of domino phase is still found in these GBs, while the simulations predict that asymmetric domino phases at inclinations $\phi < 11^\circ$ are only stable far below room temperature. This could indicate that the potential overestimates the stability of the pearl phase. However, the experimental GBs also differ from the idealized, simulated GBs in several ways. If the GB deviates from the $\Sigma 37c$ misorientation or contains small twist components, the GB phase stability will be affected and even domino/pearl phase patterning could occur [51]. Stresses and strains in the thin film or due to nearby triple junctions will also change the stability ranges of the GB phases [50], especially close to the transition point, where the excess free energy differences are small. These stresses are temperature dependent, so the occurrence of domino phase in the experimental samples is a nontrivial function of temperature. Finally, metastable domino phase may occur due to thermal fluctuations during deposition or annealing. The experimental samples are much thicker than the simulated ones, so we expect the GB transformation kinetics to be much slower [50]. We therefore cannot exclude that GB phases in experimental samples are simply prevented from transforming kinetically.

We nevertheless observe steps in domino and disconnection types I–IV in both GB phases, which confirms the simulation result that these are the most common defects with the smallest Burgers vectors. We also find the type VI defect in pearl, but not in domino. The types I/II and III/IV often appear in pairs (as discussed above), sometimes paired across different GB phases. In particular in Fig. 11(a) and (e), pairs of types I and III are observed without many compensating defect types II or IV. While the STEM images only cover a small part of the overall GB, the observed combinations add up to an overall nonzero Burgers vector, at least locally. We measured the misorientation of these GBs and found small deviations from the ideal value $\theta = 50.6^\circ$. The net Burgers vector component b_y is thus responsible for this (local) deviation.

We also present data from an Al thin film in Fig. 12. For this material, we know that the pearl phase is not observed [53, 80], so the data is limited to the domino/zipper phase. The misorientation also deviates more from $\Sigma 37c$ than in the Cu samples and our data only includes shorter segments.

We can nevertheless identify the defect types III and IV in these GBs, in accordance with the expectations from the simulation. This defect combination can lead to a net zero Burgers vector overall, as discussed before, but since b_y can

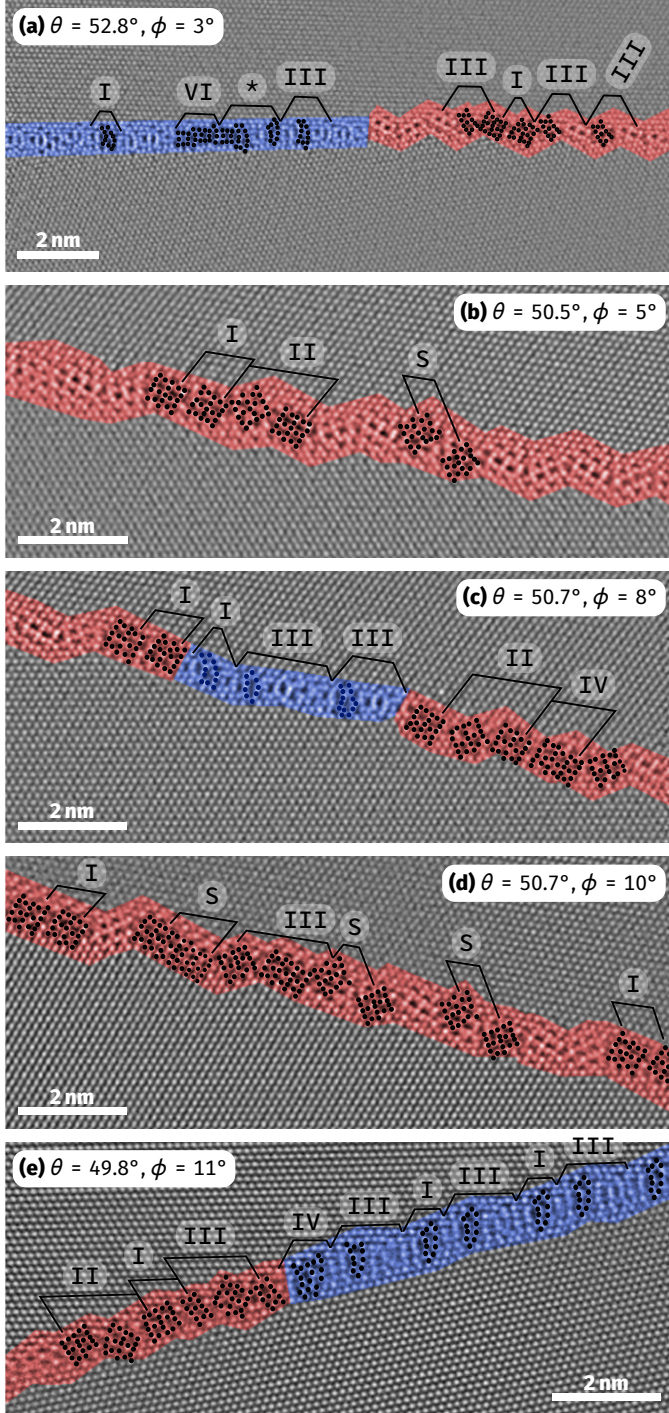


Figure 11: HAADF-STEM images of asymmetric GBs in Cu. Motifs and disconnection types are marked. GB phases are colored to indicate domino (red) and pearl (blue). Raw images are provided in Supplemental Fig. S5. The asterisk in (a) marks a segment with no overall defect character and looks like a dipole of two type I defects with opposite Burgers vector and step height. Note that (a) and (e) deviate from the perfect misorientation angle $\theta = 50.6^\circ$ and the defects add up to an overall nonzero b_y component to compensate this. The misorientation does not deviate in (d), although the visible Burgers vectors do not cancel out. However, there are many steps that do not exist in (a) and (e), so it is likely that the defects are outliers that are compensated outside the visible segment.

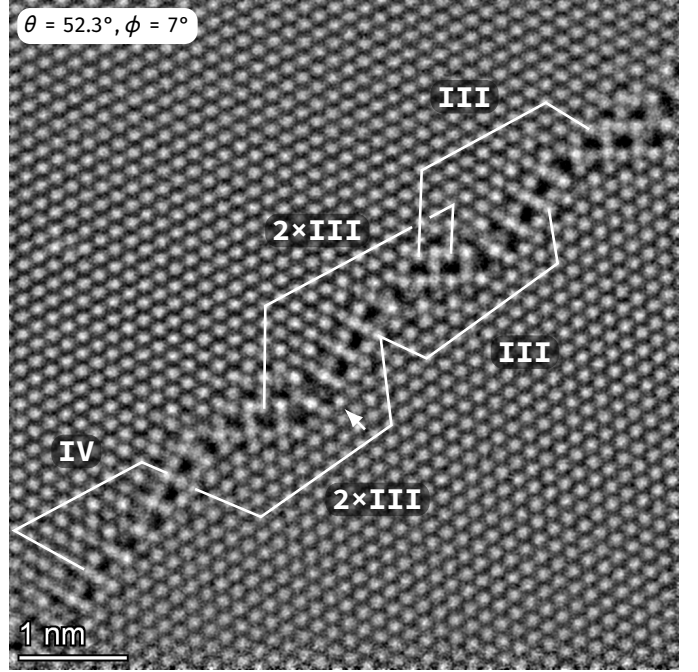


Figure 12: HAADF-STEM image of an asymmetric GB in Al. Disconnections are marked. The misorientation deviates from $\theta = 50.6^\circ$ for $\Sigma 37c$, so instead of pure steps type III and IV defects are combined such that a b_y component remains (see text). More images with similar defects are shown in Supplemental Fig. S6.

have either sign, they can also add up to $b_x = 0$ but $b_y \neq 0$. The latter is the case here and it is likely the reason that disconnections instead of steps are observed: the deviation from the perfect $\Sigma 37c$ misorientation is compensated by this b_y component. The type III defects manifest here as segments with three square motifs instead of two. We also observed a $2 \times$ III defect (double the Burgers vector and step height of type III), with three clearly visible square motifs and a less clearly-defined motif at the junction (arrow).

Overall, the predicted structures and defect types in Sec. 5.1 agree well with the present experimental observations. However, the low predicted transition temperatures in Cu (Figs. 4 and 5) cannot explain the experimental observation of the domino phase at room temperature. This might be because the interatomic potential predicts the wrong free energies, but importantly the transformation kinetics and the actual stress state also strongly influence GB phase occurrence in real samples.

5.3. High inclination angles and faceting

Beyond $\phi \approx 11^\circ$, the pearl phase can no longer compensate the inclination by introducing disconnections, while the domino phase can still have steps. The GBs with higher inclination angles must therefore either be pure domino/zipper phases or they must facet. In fact, we can also think of steps in domino/zipper as faceting (Fig. 13(a)). We notice, however, that designating steps in zipper as domino phase facets leads to very small domino facets that rather resemble steps (Fig. 13(b)). Instead of extended

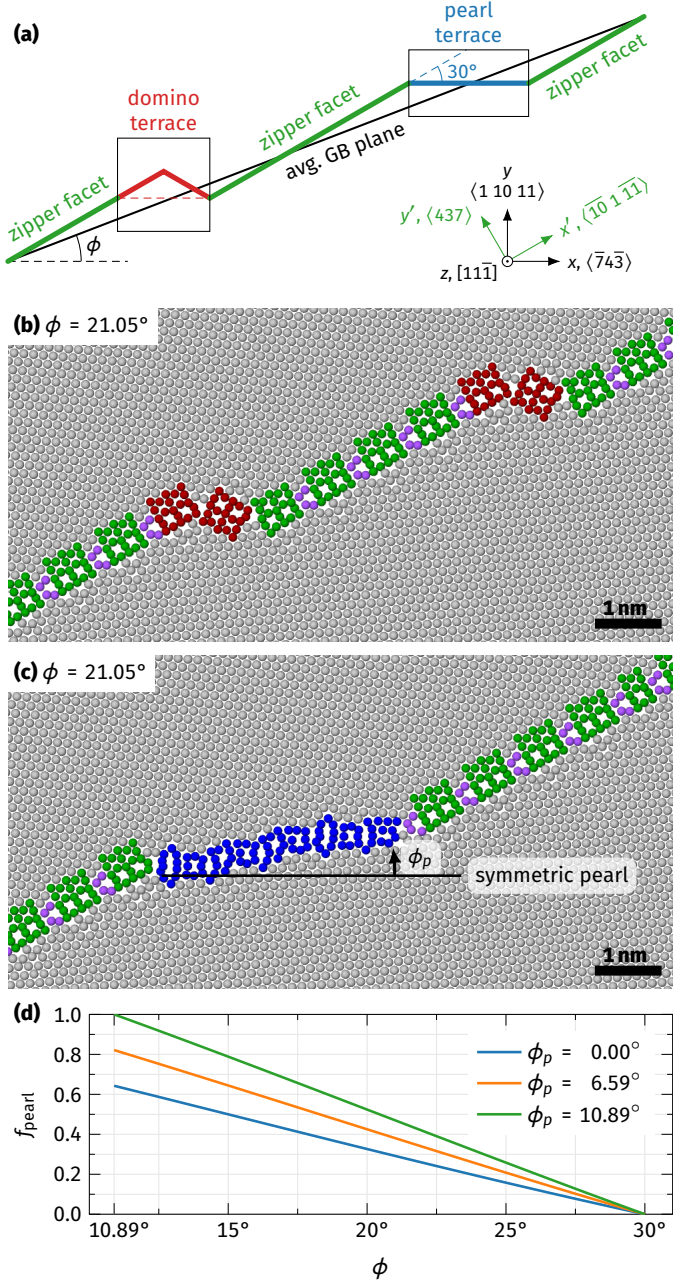


Figure 13: Inclination angles with $11^\circ < \phi < 30^\circ$ lead to faceted GBs. (a) When referencing to $\phi = 0^\circ$, we can also describe one facet as a terrace defect. There are GB phase junctions between the facet and the terrace. (b) Due to elastic interactions, the domino facets have minimal length (see text). (c) Pearl facets have a driving force to grow to minimize the number of GB phase junctions/facet junctions. The pearl facets, however, also exhibit defects to increase their inclination ϕ_p from the symmetric $\{1\ 10\ 11\}$ plane. This is due to the low energy of the pearl defects (cf. low ϕ in Fig. 3). (d) For a mix of pearl and zipper, we can geometrically estimate the fraction of pearl facets. This fraction will increase if the pearl phase is additionally inclined by ϕ_p due to its own defects.

domino facets, individual step-like defects are preferred. This is because this configuration minimizes the strain energy (see Supplemental Fig. S7) and domino/zipper facet junctions do not cost energy [81]. For pearl facets

(Fig. 13(c)), the segments are extended, because zipper/pearl phase junctions are connected with an energy cost. The pearl facet is often not defect free and deviates from $\phi = 0^\circ$.

Geometrically, the amount of pearl facets can be calculated as the fraction f_{pearl} of pearl along the average GB plane (see Supplemental, Sec. VIII for details). This depends on the inclinations of the two facets via

$$f_{\text{pearl}} = \frac{a_z \cos \phi - \cos \phi_z}{a_z \cos \phi_p - a_p \cos \phi_z} a_p, \quad (20)$$

with

$$a_p = \cos \phi_p \cos \phi + \sin \phi_p \sin \phi \quad (21)$$

$$a_z = \cos \phi_z \cos \phi + \sin \phi_z \sin \phi. \quad (22)$$

Here, ϕ is the average inclination of the GB plane, ϕ_p is the inclination of the pearl facets, and ϕ_z is the inclination of the zipper facets. As discussed in Sec. 5.1, zipper is almost defect-free and steps in zipper can be thought of as domino phase. We thus assume a fixed $\phi_z = 30^\circ$. For pearl, inclinations up to 10.89° are possible. We thus plotted three different values of ϕ_p in Fig. 13(d). For $\phi = 16.10^\circ$, the pearl fraction indeed corresponds to the predicted value (Fig. 5, gray bars). For inclinations at 21.05° , pearl still exists, but the fraction of pearl phase is lower than predicted. Instead, domino/zipper facets appear partially in their place. At even higher inclinations, we find little to no pearl phase. The GB energies in Fig. 3 explain this. The energy of the domino/zipper phase decreases sharply for higher inclinations, but the pearl facet energy should still correspond to the case of $\phi = 10.89^\circ$. The increasing energy difference thus destabilizes the pearl phase, while the region around $\phi = 21.05^\circ$ represents a transition zone where metastable mixed structures are observed.

In order to characterize the faceted structures in terms of GB defects, we can also designate the domino or pearl facets as “terrace defects” (Fig. 13(a)) and calculate their defect content with a Burgers circuit. Figure 14 shows some examples of this analysis, where the defect content relative to the zipper phase was determined. First, we note that the GB phase junctions are irrelevant to the total defect content of the terraces since they always appear in opposite pairs that cancel each other. Next, we sometimes find that a terrace has a finite Burgers vector content (red circuits in Fig. 14). These defects are always compensated by nearby defects in zipper (yellow extensions to the red circuits). Therefore, the terraces act as steps in the zipper phase, with step heights of $n \cdot 37d_y$. Macroscopically, Eq. 20 should therefore apply when the pearl facets are stable.

6. Conclusion

The relative stability of GB phases is often investigated for special or symmetric GBs. Here, we investigate asymmetric tilt GBs as a step towards understanding general GBs. For our $\Sigma 37c$ $[11\bar{1}]$ tilt GBs in Cu, we find different types of defects in the domino/zipper phase and the

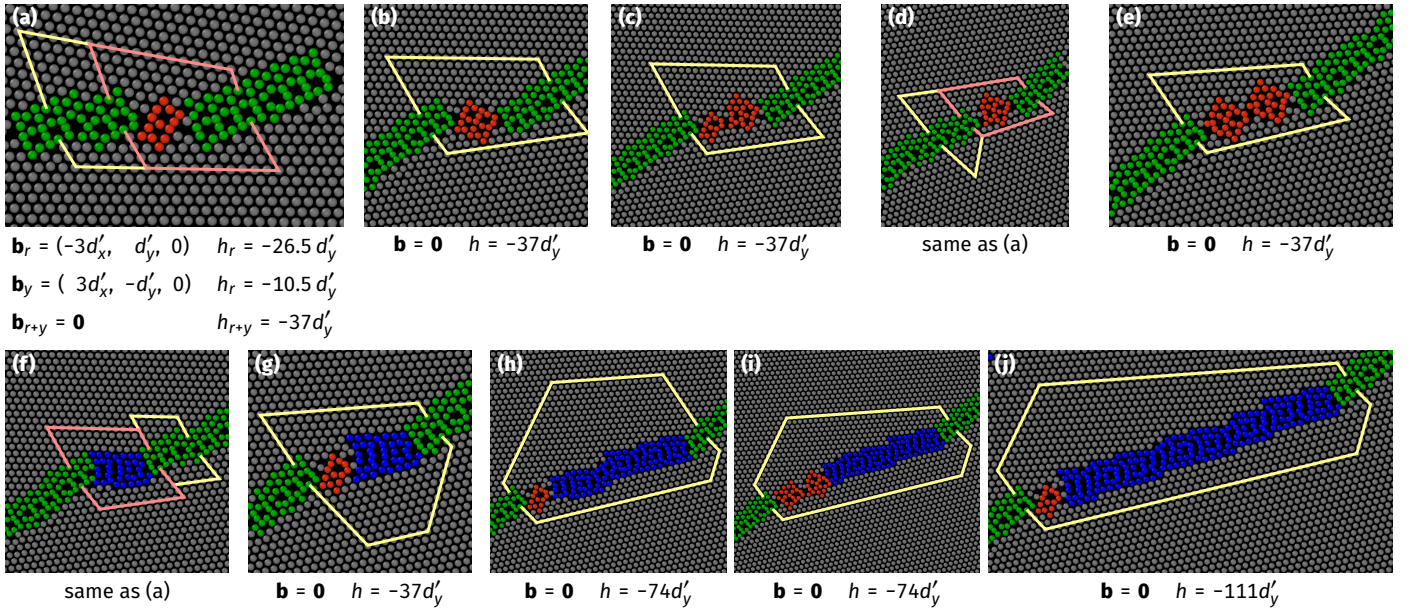


Figure 14: Analysis of some terrace-facet defects. In the panels with only a yellow Burgers circuit, the terrace overall acts as a step defect. Sometimes, there is a defect content in the terrace (red circuits, \mathbf{b}_r , h_r). This is then directly compensated by a nearby zipper type I disconnection (yellow circuit next to red circuit, \mathbf{b}_y , h_y). The terraces' disconnection mode (\mathbf{b}_y , h_y) was not observed in pure zipper (Fig. 10). Domino terraces have minimal size to minimize their elastic energy (see text).

pearl phase. The former GB phase can contain pure steps that can be combined to obtain any inclination from 0° to 30° , which is the complete range due to the crystal symmetry. For the pearl phase, different disconnections can be combined to achieve inclinations up to around 11° . Interestingly, simulations predict that the combinations of disconnections have lower defect energies than the pure steps in the domino/zipper phase. This can be explained by considering that the defect combinations have a net zero Burgers vector and also act as steps when combined. The resulting step energy is lower in the pearl phase in the present case. This leads to a significant reduction of the stability of the domino phase even at low inclinations compared to the symmetric GB plane. For inclinations above 11° , faceting of pearl and zipper phases becomes geometrically necessary and the ratios of the facets can be predicted.

A comparison to STEM experiments on Cu thin films confirms that the defect types predicted by the simulations are indeed present in real samples. Experimentally observed GBs in Al also contain similar defects, hinting that the present results could be applicable to different fcc metals. While the defect structures are modeled correctly, we however observe more domino phase in the experimental Cu sample than in the simulations. This could indicate that its stability is underestimated by the interatomic potential. Additionally, a complex stress state in the thin film sample, which also changes with temperature during post-deposition annealing, could stabilize the domino phase. Finally, the experimental sample is much thicker than the simulation model, slowing down the GB transformation kinetics and potentially leading to the appearance of residual

domino phase.

Overall, these results nevertheless clearly demonstrate that GB thermodynamics is strongly affected by geometrically necessary defects, which in turn strongly depend on the atomic structure of the GB motifs. A full understanding of GB thermodynamics consequently requires a treatment of GB line defects in addition to the free energies of the symmetric GB planes.

7. Acknowledgments

This project has received funding from the European Research Council (ERC) under the European Union's Horizon 2020 research and innovation program (Grant agreement No. 787446; GB-CORRELATE). S.S. and G.D. acknowledge partial funding from Deutsche Forschungsgemeinschaft (DFG) within SFB 1394 (project ID 409476157). Y.C. was supported by the National Research Foundation of Korea (NRF) funded by the Korea government (Ministry of Science and ICT) (No. RS-2023-00254343).

S.P. conducted most simulations and analyses. L.L. performed the STEM investigations on Cu and S.S. performed the STEM investigations on Al. Y.C. ran the structure search with GRIP. R.J., C.H.L., G.D., and T.B. contributed to the conceptualization of the study, discussions, and interpretation of the results. C.H.L. supervised the experimental investigations. G.D. secured funding via the ERC advanced Grant GB-CORRELATE and supervised the overall project. T.B. performed some analyses, designed the study, and supervised the simulations. S.P. and T.B. were responsible for drafting the manuscript, with all authors contributing to revisions.

Appendix A. Supplemental material

Supplementary material related to this article can be found online together with this article on arXiv.

References

- [1] E. O. Hall, The deformation and ageing of mild steel: III discussion of results, *Proceedings of the Physical Society. Section B* 64 (9) (1951) 747–753. [doi:10.1088/0370-1301/64/9/303](https://doi.org/10.1088/0370-1301/64/9/303).
- [2] N. J. Petch, The cleavage strength of polycrystals, *Journal of the Iron and Steel Institute* 174 (1953) 25–28.
- [3] P. Lejcek, *Grain Boundary Segregation in Metals*, Springer Series in Materials Science, Springer Berlin Heidelberg, 2010.
URL https://books.google.de/books?id=J9ZV_tbKbAKC
- [4] L. Priester, *Grain Boundaries: From Theory to Engineering*, Springer Series in Materials Science, Springer Netherlands, 2012.
URL https://books.google.de/books?id=cZAlnkgk_1oC
- [5] J. Han, S. L. Thomas, D. J. Srolovitz, Grain-boundary kinetics: A unified approach, *Progress in Materials Science* 98 (2018) 386–476. [doi:10.1016/j.pmatsci.2018.05.004](https://doi.org/10.1016/j.pmatsci.2018.05.004).
- [6] I. Kaur, Y. Mishin, W. Gust, *Fundamentals of Grain and Interphase Boundary Diffusion*, Wiley, 1995.
- [7] S. V. Divinski, H. Edelhoff, S. Prokofjev, Diffusion and segregation of silver in copper $\Sigma 5(310)$ grain boundary, *Phys. Rev. B* 85 (2012) 144104. [doi:10.1103/PhysRevB.85.144104](https://doi.org/10.1103/PhysRevB.85.144104).
URL <https://link.aps.org/doi/10.1103/PhysRevB.85.144104>
- [8] T. Frolov, S. V. Divinski, M. Asta, Y. Mishin, Effect of interface phase transformations on diffusion and segregation in high-angle grain boundaries, *Phys. Rev. Lett.* 110 (2013) 255502. [doi:10.1103/PhysRevLett.110.255502](https://doi.org/10.1103/PhysRevLett.110.255502).
URL <https://link.aps.org/doi/10.1103/PhysRevLett.110.255502>
- [9] W. E. Taylor, N. H. Odell, H. Y. Fan, Grain boundary barriers in germanium, *Phys. Rev.* 88 (1952) 867–875. [doi:10.1103/PhysRev.88.867](https://doi.org/10.1103/PhysRev.88.867).
- [10] P. V. Andrews, M. B. West, C. R. Robeson, The effect of grain boundaries on the electrical resistivity of polycrystalline copper and aluminium, *Philos. Mag.* 19 (1969) 887–898. [doi:10.1080/14786436908225855](https://doi.org/10.1080/14786436908225855).
- [11] A. F. Mayadas, M. Shatzkes, Electrical-resistivity model for polycrystalline films: the case of arbitrary reflection at external surfaces, *Phys. Rev. B* 1 (1970) 1382–1389. [doi:10.1103/PhysRevB.1.1382](https://doi.org/10.1103/PhysRevB.1.1382).
- [12] G. Lormand, Electrical properties of grain boundaries, *J. Phys. Colloques* 43 (1982) C6–283–C6–292. [doi:10.1051/jphyscol:1982625](https://doi.org/10.1051/jphyscol:1982625).
- [13] H. Bishara, S. Lee, T. Brink, M. Ghidelli, G. Dehm, Understanding grain boundary electrical resistivity in Cu: The effect of boundary structure, *ACS Nano* 15 (10) (2021) 16607–16615. [doi:10.1021/acsnano.1c06367](https://doi.org/10.1021/acsnano.1c06367).
URL <https://doi.org/10.1021/acsnano.1c06367>
- [14] P. G. Klemens, Phonon scattering and thermal resistance due to grain boundaries, *Int. J. Thermophys.* 15 (1994) 1345–1351. [doi:10.1007/BF01458842](https://doi.org/10.1007/BF01458842).
- [15] N. Goel, E. B. Webb, J. M. Rickman, A. Oztekin, S. Neti, Thermal transport across symmetric tilt grain boundaries in β -SiC: Effect of dopants and temperature, *AIP Adv.* 6 (2016) 075101. [doi:10.1063/1.4955431](https://doi.org/10.1063/1.4955431).
- [16] J. Hickman, Y. Mishin, Thermal conductivity and its relation to atomic structure for symmetrical tilt grain boundaries in silicon, *Phys. Rev. Mater.* 4 (2020) 033405. [doi:10.1103/PhysRevMaterials.4.033405](https://doi.org/10.1103/PhysRevMaterials.4.033405).
- [17] E. Isotta, S. Jiang, G. Moller, A. Zevalkink, G. J. Snyder, O. Balogun, Microscale imaging of thermal conductivity suppression at grain boundaries, *Adv. Mater.* 35 (38) (2023) 2302777. [doi:10.1002/adma.202302777](https://doi.org/10.1002/adma.202302777).
URL <https://doi.org/10.1002/adma.202302777>
- [18] E. Isotta, S. Jiang, R. Bueno-Villoro, R. Nagahiro, K. Maeda, D. A. Mattlat, A. R. Odufisan, A. Zevalkink, J. Shiomi, S. Zhang, C. Scheu, G. J. Snyder, O. Balogun, Heat transport at silicon grain boundaries, *Adv. Funct. Mater.* 34 (2024) 2405413. [doi:10.1002/adfm.202405413](https://doi.org/10.1002/adfm.202405413).
- [19] J. W. Gibbs, *The Collected Works of J. Willard Gibbs*, Volume 1: Thermodynamics, Yale University Press, New Haven, CT, USA, 1948.
- [20] E. W. Hart, Two-dimensional phase transformation in grain boundaries, *Scr. Metall.* 2 (1968) 179–182. [doi:10.1016/0036-9748\(68\)90222-6](https://doi.org/10.1016/0036-9748(68)90222-6).
- [21] J. W. Cahn, *Thermodynamics of solid and fluid surfaces*, in: W. C. Johnson, J. M. Blakely (Eds.), *Interfacial Segregation*, American Society of Metals, Metals Park, OH, USA, 1979, pp. 379–399.
URL <https://doi.org/10.1002/9781118788295.ch39>

- [22] J. W. Cahn, Transitions and phase equilibria among grain boundary structures, *Le Journal de Physique Colloques* 43 (C6) (1982) C6–199–C6–213. [doi:10.1051/jphyscol:1982619](https://doi.org/10.1051/jphyscol:1982619).
- [23] C. Rottman, Theory of phase transitions at internal interfaces, *J. Phys. Colloques* 49 (1988) C5–313–C5–326. [doi:10.1051/jphyscol:1988538](https://doi.org/10.1051/jphyscol:1988538).
- [24] T. Frolov, Y. Mishin, *Thermodynamics of coherent interfaces under mechanical stresses. i. theory*, *Phys. Rev. B* 85 (2012) 224106. [doi:10.1103/PhysRevB.85.224106](https://doi.org/10.1103/PhysRevB.85.224106).
URL <https://link.aps.org/doi/10.1103/PhysRevB.85.224106>
- [25] T. Frolov, Y. Mishin, *Thermodynamics of coherent interfaces under mechanical stresses. ii. application to atomistic simulation of grain boundaries*, *Phys. Rev. B* 85 (2012) 224107. [doi:10.1103/PhysRevB.85.224107](https://doi.org/10.1103/PhysRevB.85.224107).
URL <https://link.aps.org/doi/10.1103/PhysRevB.85.224107>
- [26] J. Han, V. Vitek, D. J. Srolovitz, The grain-boundary structural unit model redux, *Acta Materialia* 133 (2017) 186–199. [doi:10.1016/j.actamat.2017.05.002](https://doi.org/10.1016/j.actamat.2017.05.002).
- [27] T. Frolov, Y. Mishin, Phases, phase equilibria, and phase rules in low-dimensional systems, *The Journal of Chemical Physics* 143 (4) (2015) 044706. [doi:10.1063/1.4927414](https://doi.org/10.1063/1.4927414).
- [28] M. Tang, W. C. Carter, R. M. Cannon, Diffuse interface model for structural transitions of grain boundaries, *Physical Review B* 73 (2) (Jan. 2006). [doi:10.1103/physrevb.73.024102](https://doi.org/10.1103/physrevb.73.024102).
- [29] S. J. Dillon, M. Tang, W. C. Carter, M. P. Harmer, Complexion: A new concept for kinetic engineering in materials science, *Acta Materialia* 55 (18) (2007) 6208–6218. [doi:10.1016/j.actamat.2007.07.029](https://doi.org/10.1016/j.actamat.2007.07.029).
- [30] P. R. Cantwell, M. Tang, S. J. Dillon, J. Luo, G. S. Rohrer, M. P. Harmer, Grain boundary complexions, *Acta Materialia* 62 (2014) 1–48. [doi:10.1016/j.actamat.2013.07.037](https://doi.org/10.1016/j.actamat.2013.07.037).
- [31] P. R. Cantwell, T. Frolov, T. J. Rupert, A. R. Krause, C. J. Marvel, G. S. Rohrer, J. M. Rickman, M. P. Harmer, Grain boundary complexion transitions, *Annual Review of Materials Research* 50 (1) (2020) 465–492. [doi:10.1146/annurev-matsci-081619-114055](https://doi.org/10.1146/annurev-matsci-081619-114055).
- [32] S. Korte-Kerzel, T. Hickel, L. Huber, D. Raabe, S. Sandlöbes-Haut, M. Todorova, J. Neugebauer, Defect phases – thermodynamics and impact on material properties, *Int. Mater. Rev.* 67 (2022) 89–117. [doi:10.1080/09506608.2021.1930734](https://doi.org/10.1080/09506608.2021.1930734).
- [33] A. Tehranchi, S. Zhang, A. Zendegani, C. Scheu, T. Hickel, J. Neugebauer, Metastable defect phase diagrams as roadmap to tailor chemically driven defect formation, *Acta Mater.* 277 (2024) 120145. [doi:10.1016/j.actamat.2024.120145](https://doi.org/10.1016/j.actamat.2024.120145).
- [34] X. Zhou, P. Mathews, B. Berkels, W. Delis, S. Saood, A. Shamseldeen Ali Alhassan, P. Keuter, J. M. Schneider, S. Korte-Kerzel, S. Sandlöbes-Haut, D. Raabe, J. Neugebauer, G. Dehm, T. Hickel, C. Scheu, S. Zhang, Materials design by constructing phase diagrams for defects, *Adv. Mater.* 37 (2025) 2402191. [doi:10.1002/adma.202402191](https://doi.org/10.1002/adma.202402191).
- [35] J. Li, Y. Mishin, Line and planar defects with zero formation free energy: Applications of the phase rule towards ripening-immune microstructures, *Acta Mater.* 298 (2025) 121364. [doi:10.1016/j.actamat.2025.121364](https://doi.org/10.1016/j.actamat.2025.121364).
- [36] T. Frolov, M. Asta, Y. Mishin, Segregation-induced phase transformations in grain boundaries, *Phys. Rev. B* 92 (2015) 020103. [doi:10.1103/PhysRevB.92.020103](https://doi.org/10.1103/PhysRevB.92.020103).
URL <https://link.aps.org/doi/10.1103/PhysRevB.92.020103>
- [37] Z. Luo, C. Hu, L. Xie, H. Nie, C. Xiang, X. Gu, J. He, W. Zhang, Z. Yu, J. Luo, *A highly asymmetric interfacial superstructure in WC: expanding the classic grain boundary segregation and new complexion theories*, *Mater. Horiz.* 7 (1) (2020) 173–180. [doi:10.1039/C9MH00969H](https://doi.org/10.1039/C9MH00969H).
URL <http://dx.doi.org/10.1039/C9MH00969H>
- [38] T. Futazuka, R. Ishikawa, N. Shibata, Y. Ikuhara, Grain boundary structural transformation induced by co-segregation of aliovalent dopants, *Nat. Commun.* 13 (2022) 5299. [doi:10.1038/s41467-022-32935-4](https://doi.org/10.1038/s41467-022-32935-4).
- [39] R. Bueno Villoro, D. Zavanelli, C. Jung, D. A. Mattlat, R. Hatami Naderloo, N. Pérez, K. Nielsch, G. J. Snyder, C. Scheu, R. He, S. Zhang, Grain boundary phases in NbFeSb half-Heusler alloys: A new avenue to tune transport properties of thermoelectric materials, *Adv. Energy Mater.* 13 (2023) 2204321. [doi:10.1002/aenm.202204321](https://doi.org/10.1002/aenm.202204321).
- [40] V. Devulapalli, E. Chen, T. Brink, T. Frolov, C. H. Liebscher, Topological grain boundary segregation transitions, *Science* 386 (2024) 420–424. [doi:10.1126/science.adq4147](https://doi.org/10.1126/science.adq4147).
- [41] M. Mills, M. Daw, G. Thomas, F. Cosandey, *High-resolution transmission electron microscopy of grain boundaries in aluminum and correlation with atomistic calculations*, *Ultramicroscopy* 40 (3) (1992) 247–257. [doi:https://doi.org/10.1016/0304-3991\(92\)90121-Y](https://doi.org/10.1016/0304-3991(92)90121-Y).

- URL <https://www.sciencedirect.com/science/article/pii/030439919290121Y>
- [42] M. J. Mills, High resolution transmission electron microscopy and atomistic calculations of grain boundaries in metals and intermetallics, Mater. Sci. Eng. A 166 (1993) 35–50. [doi:10.1016/0921-5093\(93\)90308-2](https://doi.org/10.1016/0921-5093(93)90308-2).
- [43] T. Frolov, D. L. Olmsted, M. Asta, Y. Mishin, Structural phase transformations in metallic grain boundaries, Nature Communications 4 (1) (May 2013). [doi:10.1038/ncomms2919](https://doi.org/10.1038/ncomms2919).
- [44] J. Hickman, Y. Mishin, [Extra variable in grain boundary description](#), Phys. Rev. Mater. 1 (2017) 010601. [doi:10.1103/PhysRevMaterials.1.010601](https://doi.org/10.1103/PhysRevMaterials.1.010601)
URL <https://link.aps.org/doi/10.1103/PhysRevMaterials.1.010601>
- [45] M. Aramfard, C. Deng, Mechanically enhanced grain boundary structural phase transformation in Cu, Acta Mater. 146 (2018) 304–313. [doi:10.1016/j.actamat.2017.12.062](https://doi.org/10.1016/j.actamat.2017.12.062).
- [46] Q. Zhu, A. Samanta, B. Li, R. E. Rudd, T. Frolov, Predicting phase behavior of grain boundaries with evolutionary search and machine learning, Nature Communications 9 (1) (Feb. 2018). [doi:10.1038/s41467-018-02937-2](https://doi.org/10.1038/s41467-018-02937-2).
- [47] T. Frolov, W. Setyawan, R. J. Kurtz, J. Marian, A. R. Oganov, R. E. Rudd, Q. Zhu, [Grain boundary phases in bcc metals](#), Nanoscale 10 (2018) 8253–8268. [doi:10.1039/C8NR00271A](https://doi.org/10.1039/C8NR00271A)
URL <http://dx.doi.org/10.1039/C8NR00271A>
- [48] T. Frolov, Q. Zhu, T. Oppelstrup, J. Marian, R. E. Rudd, [Structures and transitions in bcc tungsten grain boundaries and their role in the absorption of point defects](#), Acta Materialia (2018).
URL <https://api.semanticscholar.org/CorpusID:59426862>
- [49] C. Yang, M. Zhang, L. Qi, [Grain boundary structure search by using an evolutionary algorithm with effective mutation methods](#), Computational Materials Science 184 (2020) 109812. [doi:https://doi.org/10.1016/j.commatsci.2020.109812](https://doi.org/10.1016/j.commatsci.2020.109812)
URL <https://www.sciencedirect.com/science/article/pii/S0927025620303037>
- [50] T. Meiners, T. Frolov, R. E. Rudd, G. Dehm, C. H. Liebscher, Observations of grain-boundary phase transformations in an elemental metal, Nature 579 (7799) (2020) 375–378. [doi:10.1038/s41586-020-2082-6](https://doi.org/10.1038/s41586-020-2082-6).
- [51] L. Langenohl, T. Brink, R. Freitas, T. Frolov, G. Dehm, C. H. Liebscher, Dual phase patterning during a congruent grain boundary phase transition in elemental copper, Nature Communications 13 (1) (2022) 3331. [doi:10.1038/s41467-022-30922-3](https://doi.org/10.1038/s41467-022-30922-3).
- [52] I. S. Winter, R. E. Rudd, T. Oppelstrup, T. Frolov, Nucleation of grain boundary phases, Phys. Rev. Lett. 128 (2022) 035701. [doi:10.1103/PhysRevLett.128.035701](https://doi.org/10.1103/PhysRevLett.128.035701).
- [53] T. Brink, L. Langenohl, H. Bishara, G. Dehm, Universality of grain boundary phases in fcc metals: Case study on high-angle [111] symmetric tilt grain boundaries, Physical Review B 107 (5) (2023) 054103. [doi:10.1103/physrevb.107.054103](https://doi.org/10.1103/physrevb.107.054103).
- [54] E. Chen, T. W. Heo, B. C. Wood, M. Asta, T. Frolov, [Grand canonically optimized grain boundary phases in hexagonal close-packed titanium](#), Nature Communications 15 (1) (2024) 7049. [doi:10.1038/s41467-024-51330-9](https://doi.org/10.1038/s41467-024-51330-9)
URL <https://doi.org/10.1038/s41467-024-51330-9>
- [55] Y. Choi, T. Brink, Faceting transition in aluminum as a grain boundary phase transition, Phys. Rev. Mater. 9 (2025) 083607. [doi:10.1103/2dnf-zdz8](https://doi.org/10.1103/2dnf-zdz8).
- [56] T. Frolov, Effect of interfacial structural phase transitions on the coupled motion of grain boundaries: A molecular dynamics study, Applied Physics Letters 104 (21) (2014) 211905. [doi:10.1063/1.4880715](https://doi.org/10.1063/1.4880715).
- [57] S. Pemma, R. Janisch, G. Dehm, T. Brink, [Effect of the atomic structure of complexions on the active disconnection mode during shear-coupled grain boundary motion](#), Phys. Rev. Mater. 8 (2024) 063602. [doi:10.1103/PhysRevMaterials.8.063602](https://doi.org/10.1103/PhysRevMaterials.8.063602)
URL <https://link.aps.org/doi/10.1103/PhysRevMaterials.8.063602>
- [58] A. Morawiec, On ‘interface-plane scheme’ and symmetric grain boundaries, Z. Kristallogr. 227 (4) (2012) 199–206. [doi:10.1524/zkri.2012.1475](https://doi.org/10.1524/zkri.2012.1475).
- [59] T. Y. T. Wilfried R. Wagner, R. W. Balluffi, [Faceting of high-angle grain boundaries in the coincidence lattice](#), The Philosophical Magazine: A Journal of Theoretical Experimental and Applied Physics 29 (4) (1974) 895–904. [arXiv:https://doi.org/10.1080/14786437408222078](https://doi.org/10.1080/14786437408222078), [doi:10.1080/14786437408222078](https://doi.org/10.1080/14786437408222078).
URL <https://doi.org/10.1080/14786437408222078>
- [60] A. Brokman, P. Bristowe, R. Balluffi, [Atomistic faceting of assymetric tilt boundaries](#), Scripta Metallurgica 15 (2) (1981) 201–206. [doi:https://doi.org/10.1016/0036-9748\(81\)90329-X](https://doi.org/10.1016/0036-9748(81)90329-X)
URL <https://www.sciencedirect.com/science/article/pii/003697488190329X>

- [61] A. P. Sutton, V. Vitek, On the structure of tilt grain boundaries in cubic metals II. Asymmetrical tilt boundaries, *Phil. Trans. R. Soc. Lond. A* 309 (1506) (1983) 37–54. [doi:10.1098/rsta.1983.0021](https://doi.org/10.1098/rsta.1983.0021).
- [62] U. Dahmen, K. H. Westmacott, TEM characterization of grain boundaries in mazed bicrystal films of aluminum, *MRS Online Proceedings Library* 229 (1991) 167–178. [doi:10.1557/proc-229-167](https://doi.org/10.1557/proc-229-167).
- [63] B. B. Straumal, S. A. Polyakov, E. Bischoff, W. Gust, E. J. Mittemeijer, Faceting of σ_3 and σ_9 grain boundaries in copper, *Interface Science* 9 (3) (2001) 287–292.
- [64] J. A. Brown, Y. Mishin, *Dissociation and faceting of asymmetrical tilt grain boundaries: Molecular dynamics simulations of copper*, *Phys. Rev. B* 76 (2007) 134118. [URL https://doi.org/doi/10.1103/PhysRevB.76.134118](https://doi.org/10.1103/PhysRevB.76.134118)
- [65] M. A. Tschopp, D. L. McDowell, *Asymmetric tilt grain boundary structure and energy in copper and aluminium*, *Philosophical Magazine* 87 (25) (2007) 3871–3892. [arXiv: https://doi.org/10.1080/14786430701455321](https://arxiv.org/abs/https://doi.org/10.1080/14786430701455321), [doi:10.1080/14786430701455321](https://doi.org/10.1080/14786430701455321). [URL https://doi.org/10.1080/14786430701455321](https://doi.org/10.1080/14786430701455321)
- [66] M. A. Tschopp, D. L. McDowell, Structures and energies of σ_3 asymmetric tilt grain boundaries in copper and aluminium, *Philos. Mag.* 87 (2007) 3147–3173. [doi:10.1080/14786430701255895](https://doi.org/10.1080/14786430701255895).
- [67] A. D. Banadaki, S. Patala, A simple faceting model for the interfacial and cleavage energies of Σ_3 grain boundaries in the complete boundary plane orientation space, *Comput. Mater. Sci.* 112 (2016) 147–160. [doi:10.1016/j.commatsci.2015.09.062](https://doi.org/10.1016/j.commatsci.2015.09.062).
- [68] F. Abdeljawad, D. L. Medlin, J. A. Zimmerman, K. Hattar, S. M. Foiles, A diffuse interface model of grain boundary faceting, *J. Appl. Phys.* 119 (2016) 235306. [doi:10.1063/1.4954066](https://doi.org/10.1063/1.4954066).
- [69] D. L. Medlin, K. Hattar, J. A. Zimmerman, F. Abdeljawad, S. M. Foiles, Defect character at grain boundary facet junctions: Analysis of an asymmetric $\Sigma = 5$ grain boundary in Fe, *Acta Mater.* 124 (2017) 383–396. [doi:10.1016/j.actamat.2016.11.017](https://doi.org/10.1016/j.actamat.2016.11.017).
- [70] B. Dobrovolski, C. B. Owens, G. L. W. Hart, E. R. Homer, B. Runnels, Facet and energy predictions in grain boundaries: Lattice matching and molecular dynamics, *Acta Mater.* 274 (2024) 119962. [doi:10.1016/j.actamat.2024.119962](https://doi.org/10.1016/j.actamat.2024.119962).
- [71] H. Ding, A. Akbari, E. Chen, H. Rösner, T. Frolov, S. Divinski, G. Wilde, C. H. Liebscher, Hierarchy of defects in near- Σ_5 tilt grain boundaries in copper studied by length-scale bridging electron microscopy, *Acta Mater.* 287 (2025) 120778. [doi:10.1016/j.actamat.2025.120778](https://doi.org/10.1016/j.actamat.2025.120778).
- [72] Z. Trautt, A. Adland, A. Karma, Y. Mishin, Coupled motion of asymmetrical tilt grain boundaries: Molecular dynamics and phase field crystal simulations, *Acta Materialia* 60 (19) (2012) 6528–6546. [doi:10.1016/j.actamat.2012.08.018](https://doi.org/10.1016/j.actamat.2012.08.018).
- [73] C. P. Race, R. Hadian, J. von Pezold, B. Grabowski, J. Neugebauer, Mechanisms and kinetics of the migration of grain boundaries containing extended defects, *Physical Review B* 92 (17) (Nov. 2015). [doi:10.1103/physrevb.92.174115](https://doi.org/10.1103/physrevb.92.174115).
- [74] R. Hadian, B. Grabowski, C. P. Race, J. Neugebauer, Atomistic migration mechanisms of atomically flat, stepped, and kinked grain boundaries, *Phys. Rev. B* 94 (2016) 165413. [doi:10.1103/PhysRevB.94.165413](https://doi.org/10.1103/PhysRevB.94.165413). [URL https://doi.org/doi/10.1103/PhysRevB.94.165413](https://doi.org/10.1103/PhysRevB.94.165413)
- [75] T. Meiners, J. M. Duarte, G. Richter, G. Dehm, C. H. Liebscher, Tantalum and zirconium induced structural transitions at complex [111] tilt grain boundaries in copper, *Acta Mater.* 190 (2020) 93–104. [doi:10.1016/j.actamat.2020.02.064](https://doi.org/10.1016/j.actamat.2020.02.064).
- [76] S. Saood, T. Brink, C. H. Liebscher, G. Dehm, *Microstates and defects of incoherent Σ_3 [111] twin boundaries in aluminum*, *Acta Materialia* 243 (2023) 118499. [doi:https://doi.org/10.1016/j.actamat.2022.118499](https://doi.org/https://doi.org/10.1016/j.actamat.2022.118499). [URL https://www.sciencedirect.com/science/article/pii/S135964542200876X](https://doi.org/https://www.sciencedirect.com/science/article/pii/S135964542200876X)
- [77] A. Paul, T. Laurila, V. Vuorinen, S. V. Divinski, *Thermodynamics, Diffusion and the Kirkendall Effect in Solids*, Springer, Cham, CH, 2014. [doi:10.1007/978-3-319-07461-0](https://doi.org/10.1007/978-3-319-07461-0).
- [78] S. V. Sevlikar, G. M. Muralikrishna, D. Gaertner, S. Starikov, T. Brink, D. Scheiber, D. Smirnova, D. Irmer, B. Tas, V. A. Esin, V. I. Razumoskiy, C. H. Liebscher, G. Wilde, S. V. Divinski, Grain boundary diffusion and segregation of Cr in Ni Σ_{11} ($\bar{1}13$) [110] bicrystals: Decoding the role of grain boundary defects, *Acta Mater.* 278 (2024) 120229. [doi:10.1016/j.actamat.2024.120229](https://doi.org/10.1016/j.actamat.2024.120229).
- [79] L. Langenohl, T. Brink, G. Richter, G. Dehm, C. H. Liebscher, *Atomic-resolution observations of silver segregation in a [111] tilt grain boundary in copper*, *Phys. Rev. B* 107 (2023) 134112. [doi:10.1103/PhysRevB.107.134112](https://doi.org/10.1103/PhysRevB.107.134112).

- URL <https://link.aps.org/doi/10.1103/PhysRevB.107.134112>
- [80] S. Saood, T. Brink, C. H. Liebscher, G. Dehm, Influence of variation in grain boundary parameters on the evolution of atomic structure and properties of [111] tilt boundaries in aluminum, *Acta Materialia* 268 (2024) 119732. doi:<https://doi.org/10.1016/j.actamat.2024.119732>.
URL <https://www.sciencedirect.com/science/article/pii/S1359645424000855>
- [81] T. Brink, L. Langenohl, S. Pemma, C. H. Liebscher, G. Dehm, Stable nanofacets in [111] tilt grain boundaries of face-centered cubic metals, *Phys. Rev. Mater.* 8 (2024) 063606. doi:<https://doi.org/10.1103/PhysRevMaterials.8.063606>
URL <https://link.aps.org/doi/10.1103/PhysRevMaterials.8.063606>
- [82] Y. Mishin, M. J. Mehl, D. A. Papaconstantopoulos, A. F. Voter, J. D. Kress, Structural stability and lattice defects in copper: *Ab initio*, tight-binding, and embedded-atom calculations, *Physical Review B* 63 (22) (May 2001). doi:[10.1103/physrevb.63.224106](https://doi.org/10.1103/physrevb.63.224106).
- [83] S. Plimpton, Fast parallel algorithms for short-range molecular dynamics, *Journal of Computational Physics* 117 (1) (1995) 1–19. doi:[10.1006/jcph.1995.1039](https://doi.org/10.1006/jcph.1995.1039).
- [84] A. P. Thompson, H. M. Aktulga, R. Berger, D. S. Bolintineanu, W. M. Brown, P. S. Crozier, P. J. in 't Veld, A. Kohlmeyer, S. G. Moore, T. D. Nguyen, R. Shan, M. J. Stevens, J. Tranchida, C. Trott, S. J. Plimpton, LAMMPS - a flexible simulation tool for particle-based materials modeling at the atomic, meso, and continuum scales, *Computer Physics Communications* 271 (2022) 108171.
- [85] R. Freitas, M. Asta, M. de Koning, Nonequilibrium free-energy calculation of solids using LAMMPS, *Computational Materials Science* 112 (2016) 333–341. doi:<https://doi.org/10.1016/j.commatsci.2015.10.050>.
URL <https://www.sciencedirect.com/science/article/pii/S0927025615007089>
- [86] S. M. Foiles, Evaluation of harmonic methods for calculating the free energy of defects in solids, *Phys. Rev. B* 49 (1994) 14930–14938. doi:<https://doi.org/10.1103/PhysRevB.49.14930>
URL <https://link.aps.org/doi/10.1103/PhysRevB.49.14930>
- [87] R. Freitas, R. E. Rudd, M. Asta, T. Frolov, Free energy of grain boundary phases: Atomistic calculations for $\Sigma 5$ (310)[001] grain boundary in cu, *Phys. Rev. Mater.* 2 (2018) 093603.
doi:[10.1103/PhysRevMaterials.2.093603](https://doi.org/10.1103/PhysRevMaterials.2.093603).
URL <https://link.aps.org/doi/10.1103/PhysRevMaterials.2.093603>
- [88] H.-S. Nam, D. J. Srolovitz, Effect of material properties on liquid metal embrittlement in the Al–Ga system, *Acta Mater.* 57 (5) (2009) 1546–1553. doi:[10.1016/j.actamat.2008.11.041](https://doi.org/10.1016/j.actamat.2008.11.041).
- [89] W. T. Read, W. Shockley, Dislocation models of crystal grain boundaries, *Phys. Rev.* 78 (1950) 275–289. doi:<https://doi.org/10.1103/PhysRev.78.275>
URL <https://link.aps.org/doi/10.1103/PhysRev.78.275>
- [90] R. Pond, TEM studies of line defects in interfaces, *Ultramicroscopy* 30 (1-2) (1989) 1–7. doi:[10.1016/0304-3991\(89\)90165-4](https://doi.org/10.1016/0304-3991(89)90165-4).
- [91] T. Frolov, D. L. Medlin, M. Asta, Dislocation content of grain boundary phase junctions and its relation to grain boundary excess properties, *Physical Review B* 103 (18) (May 2021). doi:[10.1103/physrevb.103.184108](https://doi.org/10.1103/physrevb.103.184108).
- [92] A. Stukowski, Visualization and analysis of atomistic simulation data with ovito - the open visualization tool, *Modelling and Simulation in Materials Science and Engineering* 18 (1) (2009) 015012. doi:[10.1088/0965-0393/18/1/015012](https://doi.org/10.1088/0965-0393/18/1/015012).
- [93] N. Deka, A. Stukowski, R. B. Sills, Automated extraction of interfacial dislocations and disconnections from atomistic data, *Acta Mater.* 256 (2023) 119096. doi:[10.1016/j.actamat.2023.119096](https://doi.org/10.1016/j.actamat.2023.119096).
- [94] W. Bollmann, *Crystal Defects and Crystalline Interfaces*, Springer, 1970. doi:[10.1007/978-3-642-49173-3](https://doi.org/10.1007/978-3-642-49173-3).
- [95] R. C. Pond, D. A. Smith, On the absorption of dislocations by grain boundaries, *Philos. Mag.* 36 (1977) 353–366. doi:[10.1080/14786437708244939](https://doi.org/10.1080/14786437708244939).
- [96] A. H. King, D. A. Smith, The effects on grain-boundary processes of the steps in the boundary plane associated with the cores of grain-boundary dislocations, *Acta Crystallographica Section A* 36 (3) (1980) 335–343. doi:[10.1107/S0567739480000782](https://doi.org/10.1107/S0567739480000782).
URL <https://doi.org/10.1107/S0567739480000782>
- [97] L. Wang, J. Teng, P. Liu, A. Hirata, E. Ma, Z. Zhang, M. Chen, X. Han, Grain rotation mediated by grain boundary dislocations in nanocrystalline platinum, *Nature Communications* 5 (1) (Jul. 2014). doi:[10.1038/ncomms5402](https://doi.org/10.1038/ncomms5402).
- [98] Y. Tian, X. Gong, M. Xu, C. Qiu, Y. Han, Y. Bi, L. V. Estrada, E. Boltynjuk, H. Hahn, J. Han,

- D. J. Srolovitz, X. Pan, Grain rotation mechanisms in nanocrystalline materials: Multiscale observations in pt thin films, *Science* 386 (6717) (2024) 49–54. [arXiv:https://www.science.org/doi/pdf/10.1126/science.adk6384](https://www.science.org/doi/pdf/10.1126/science.adk6384), [doi:10.1126/science.adk6384](https://doi.org/10.1126/science.adk6384).
 URL <https://www.science.org/doi/abs/10.1126/science.adk6384>
- [99] F. Frank, The resultant content of dislocations in an arbitrary intercrystalline boundary, in: Symposium on the plastic deformation of crystalline solids, Office of Naval Research Pittsburgh, Pennsylvania, 1950, pp. 150–154.
- [100] B. Bilby, Types of dislocation source, in: Report of Bristol conference on defects in crystalline solids, The Physical Society, Bristol, 1954 London, 1955, pp. 124–133.
- [101] M. F. Ashby, On interface-reaction control of Nabarro-Herring creep and sintering, *Scr. Metall.* 3 (1969) 837–842. [doi:10.1016/0036-9748\(69\)90191-4](https://doi.org/10.1016/0036-9748(69)90191-4).
- [102] R. Balluffi, S. Allen, W. Carter, *Kinetics of Materials*, Wiley, 2005.
 URL <https://books.google.de/books?id=QNTxYPvovCEC>
- [103] J. W. Cahn, Y. Mishin, A. Suzuki, Coupling grain boundary motion to shear deformation, *Acta Materialia* 54 (19) (2006) 4953–4975. [doi:10.1016/j.actamat.2006.08.004](https://doi.org/10.1016/j.actamat.2006.08.004).
- [104] A. Rajabzadeh, F. Mompiou, M. Legros, N. Combe, Elementary mechanisms of shear-coupled grain boundary migration, *Physical Review Letters* 110 (26) (Jun. 2013). [doi:10.1103/physrevlett.110.265507](https://doi.org/10.1103/physrevlett.110.265507).
- [105] M. Larranaga, F. Mompiou, M. Legros, N. Combe, Role of sessile disconnection dipoles in shear-coupled grain boundary migration, *Physical Review Materials* 4 (12) (Dec. 2020). [doi:10.1103/physrevmaterials.4.123606](https://doi.org/10.1103/physrevmaterials.4.123606).
- [106] I. S. Winter, T. Frolov, Phase pattern formation in grain boundaries, *Phys. Rev. Lett.* 132 (2024) 186204. [doi:10.1103/PhysRevLett.132.186204](https://doi.org/10.1103/PhysRevLett.132.186204).
 URL <https://link.aps.org/doi/10.1103/PhysRevLett.132.186204>